



Published in final edited form as:

Nature. 2019 June ; 570(7761): 338–343. doi:10.1038/s41586-019-1295-z.

Structural mechanism for NEK7-licensed NLRP3 inflammasome activation

Humayun Sharif^{1,2,7}, Li Wang^{1,2,7}, Wei Li Wang^{1,2,3,4,5,7}, Venkat Giri Magupalli^{1,2}, Liudmila Andreeva^{1,2}, Qi Qiao^{1,2}, Arthur V. Hauenstein^{1,2}, Zhaolong Wu³, Gabriel Nunez⁶, Youdong Mao^{3,4,5,*}, Hao Wu^{1,2,*}

¹Department of Biological Chemistry and Molecular Pharmacology, Harvard Medical School, Boston, MA 02115

²Program in Cellular and Molecular Medicine, Boston Children's Hospital, Boston, MA 02115

³State Key Laboratory for Artificial Microstructures and Mesoscopic Physics, School of Physics, Center for Quantitative Biology, Peking University, Beijing, 100871, China

⁴Intel Parallel Computing Center for Structural Biology, Dana-Farber Cancer Institute, Boston, MA 02215, USA

⁵Department of Cancer Immunology and Virology, Dana-Farber Cancer Institute, Department of Microbiology, Harvard Medical School, Boston, MA 02115, USA

⁶Department of Pathology and Comprehensive Cancer Center, University of Michigan Medical School, Ann Arbor, MI 48109

⁷These authors contributed equally.

Summary

The NLRP3 inflammasome can be activated by diverse stimuli, including nigericin, uric acid crystals, amyloid- β fibrils, and extracellular ATP. The mitotic kinase NEK7 licenses NLRP3 inflammasome assembly and activation in the interphase. Here we report a 3.8-Å cryo-electron microscopy structure of inactive human NLRP3 in complex with NEK7. The earring-shaped

Users may view, print, copy, and download text and data-mine the content in such documents, for the purposes of academic research, subject always to the full Conditions of use:http://www.nature.com/authors/editorial_policies/license.html#terms

*Correspondence: wu@crystal.harvard.edu; yao@pku.edu.cn.

Author Contributions H.W., L.W. and H.S. conceived the study. L.W. designed constructs. L.W., Q.Q. and H.S. purified the complexes, and H.S., L.W. and Q.Q. made cryo-grids for data collection. H.S., L.W., W.L.W., Q.Q., Z.W. and Y.M. collected data. H.S., W.L.W. and Q.Q. analysed cryo-EM data and H.W. and Y.M. supervised data processing. H.S. performed initial model building and refinement, and W.L.W. and Y.M. performed additional model fitting and refinement. H.S. designed mutants for *in vitro* and cell based assays. V.G.M. performed all cell-based assays. L.A. and A.V.H. performed NEK7 mutant assays. G.N. provided reagents for cell based assays and valuable discussions. H.W., H.S. and Y.M. wrote the manuscript, and all authors provided comments on the manuscript.

Author Information Reprints and permissions information is available at www.nature.com/reprints. The authors declare competing financial interests: L.W. and A.V.H. are employees and H.W. is co-founder of SMOC Therapeutics; other authors declare no competing interests. Readers are welcome to comment on the online version of the paper. Correspondence and requests for materials should be addressed to H.W. (wu@crystal.harvard.edu) or Y.M. (yao@pku.edu.cn).

Data availability.

The cryo-EM map has been deposited in the Electron Microscopy Data Bank under the accession number EMD-0476. The atomic coordinates have been deposited in the Protein Data Bank under the accession number 6NPY. All other data can be obtained from the corresponding author upon reasonable request.

NLRP3 consists of curved leucine-rich repeat (LRR) and globular NACHT domains, whereas the C-terminal lobe of NEK7 nestles against both NLRP3 domains. Structural recognition between NLRP3 and NEK7 is confirmed by mutagenesis both in vitro and in cells. Modelling of an active NLRP3-NEK7 conformation based on the NLRC4 inflammasome predicts an additional contact between an NLRP3-bound NEK7 and a neighbouring NLRP3. Mutations on this interface abolish the ability of NEK7 or NLRP3 to rescue NLRP3 activation in NEK7^{KO} or NLRP3^{KO} cells. Taken together, these data suggest that NEK7 bridges adjacent NLRP3 subunits with bipartite interactions to mediate NLRP3 inflammasome activation.

Inflammasomes are cytoplasmic supramolecular complexes that form in response to exogenous microbial invasions and endogenous damage signals¹⁻³. Inflammasomes activate inflammatory caspases such as caspase-1, which processes proinflammatory cytokines interleukin 1 β (IL-1 β) and IL-18 for their maturation, and cleaves the gasdermin D to generate the N-terminal fragment to induce pore formation, cytokine release and pyroptotic cell death^{2,4,5}. NLRP3 belongs to the family of nucleotide-binding domain (NBD) and leucine-rich repeat (LRR)-containing proteins (NLRs). It has an N-terminal Pyrin domain (PYD), which interacts with the adapter protein ASC via PYD-PYD interactions, a central adenosine triphosphatase (ATPase) domain known as NACHT that comprises NBD, helical domain 1 (HD1), winged helix domain (WHD) and helical domain 2 (HD2), and a C-terminal LRR domain⁶ (Fig. 1a). ASC also has a caspase recruitment domain (CARD) that recruits caspase-1 via CARD-CARD interactions to promote caspase dimerization and activation. Our previous studies revealed that PYDs and CARDS both form filamentous assemblies through nucleated polymerization⁷⁻⁹. NLRP3 is an extensively studied inflammasome sensor activated by a spectrum of seemingly unrelated stimuli via induction of K⁺ efflux^{1-3,10-12}. Autosomal-dominant mutations of the *NLRP3* gene are related to autoinflammatory diseases, which are collectively known as cryopyrin-associated periodic syndromes (CAPS); NLRP3 hyperactivation is directly connected to systematic and joint inflammation^{1-3,10}. Several groups recently identified the mitotic Ser/Thr kinase NEK7 as an important requirement in NLRP3 activation via direct NLRP3-NEK7 interaction¹³⁻¹⁶. Because of its interaction with NEK9 during mitosis and its limited quantity in cells, NEK7 licenses NLRP3 activation only in interphase¹⁶. However, the molecular mechanism of the NLRP3-NEK7 interaction remains unknown.

Cryo-EM structure determination

We expressed and purified a recombinant complex of PYD-deleted, maltose-binding protein (MBP)-tagged NLRP3 (NLRP3^{-PYD}) with NEK7. Microscale thermophoresis (MST) showed a dissociation constant of 78.9 ± 38.5 nM between NLRP3 and NEK7 (Fig. 1b, Extended Data Fig. 1a). Thermal shift assay indicated that the NLRP3 inhibitor, MCC950¹⁷ and ADP both increased the stability of NLRP3 or of the complex, but not of NEK7 alone (Extended Data Fig. 1b-d). Cryo-EM images of the complex, however, showed poor contrast, likely due to the relatively small size of the complex (~185 kD with the MBP tag).

To facilitate structure determination, we generated an artificial NEK7 dimer based on a dimer structure of protein kinase R (PKR) (PDB ID: 2A19)¹⁸ (Extended Data Fig. 1e). The

engineered NEK7 formed a dimeric complex with NLRP3, as shown by a shift in the elution position from a gel filtration column and by multi-angle light scattering (MALS) measurements (Fig. 1c–d, Extended Data Fig. 1f). Although dimeric in solution, 2D classification revealed mostly monomeric NLRP3-NEK7 particles, suggesting that the two complexes in the dimer are flexibly linked. We speculate that despite the flexibility, the larger dimer complexes facilitated particle picking and 3D reconstruction. Cryo-EM analysis was first conducted using a Talos Arctica microscope, resulting in a 4.3-Å reconstruction (Extended Data Fig. 2a–d, Extended Data Table 1). A larger cryo-EM data set containing 15,681 movies collected on a Titan Krios microscope (Extended Data Fig. 2e) gave rise to the final 3.8-Å map refined with 108,771 particles selected from multiple rounds of 2D/3D classifications (Fig. 1e–f, Extended Data Fig. 2e–g, Extended Data Table 1). The data included 1,340 movies collected at a stage tilt of 20°, which improved particle orientation distribution (Extended Data Fig. 2f).

Atomic model building was initially performed on the 4.3-Å map, which was assisted by structures of other NLRs and NEK7, and was finalized on the 3.8-Å map (Fig. 2a, Extended Data Fig. 3). The map revealed an earring shape characteristic of NLRs such as NLRC4^{6,19,20}, NOD2²¹ and NAIP5^{22,23}, containing a curved LRR domain and a compact NACHT comprising NBD, HD1, WHD and HD2 (Fig. 2a). The LRR region comprises 12 repeats, consistent with the structure prediction using Phyre2²⁴ (Extended Data Fig. 4). The density encircled by the LRR was fitted well with the C-terminal lobe of the crystal structure of human NEK7 (PDB ID 2WQN)²⁵ as a rigid body. No density was visible for the N-terminal lobe of NEK7 (Extended Data Fig. 3a, 3h), likely because the mutations introduced to this region to generate a NEK7 dimer might have affected the structural integrity of NEK7 N-lobe.

Overall structure of the complex and interactions

The final atomic model contains almost the entire NLRP3 (without the N-terminal MBP), the NEK7 C-lobe and the ADP bound to the NBD of NLRP3 (Fig. 2a, Extended Data Table 1, Supplementary Video 1). When the full-length NEK7 structure is overlaid with the NLRP3-NEK7 model, the N-lobe extends away from the complex with no steric hindrance against NLRP3 (Extended Data Fig. 5a). The activation loop including S195 whose phosphorylation activates NEK7 is disordered in the NLRP3-NEK7 complex and does not contact NLRP3 (Extended Data Fig. 5b), consistent with the observation that both active and inactive NEK7 can support NLRP3 activation^{13–15}. The NBD-HD1-WHD module of NLRP3 exhibited a conformation similar to the inactive conformation of NLRC4 and NOD2, whereas the HD2 and LRR structures are variable among the known structures in the NLR family (Extended Data Fig. 5c–e). Interestingly, NEK7 binds an LRR region where the phosphorylated S533 residue of NLRC4 interacts intramolecularly, although the role of S533 phosphorylation in NLRC4 activation remains controversial^{6,26,27} (Extended Data Fig. 5e).

NLRP3 interacts with NEK7 at multiple surfaces including LRR, HD2 and NBD (Extended Data Fig. 6–7). The calculated isoelectric points (pI) of NEK7 and NLRP3 are 8.5 and 6.2, making NEK7 and NLRP3 positively and negatively charged overall at physiological pH,

respectively (Fig. 2b). The NEK7 C-lobe is even more positively charged, with a calculated pI of 9.0. Indeed, the interaction between NLRP3 and NEK7 is dictated partly by electrostatic complementarity (Fig. 2b). The positively charged nature of NEK7 is also reflected in the bound SO_4 ion in its crystal structure²⁵, at its interface with NLRP3 (Extended Data Fig. 8a). The interactions between NLRP3 and NEK7 can be divided into two interfaces: those between LRR of NLRP3 and the first half of the NEK7 C-lobe (Fig. 3a–b, Extended Data Fig. 8b) and those between NACHT (NBD and HD2) and the second half of the NEK7 C-lobe (Fig. 3a, 3c, Extended Data Fig. 8b). They bury surface areas of $\sim 880 \text{ \AA}^2$ and $\sim 770 \text{ \AA}^2$, respectively.

Structural insights into NEK7 for NLRP3 interaction

On NEK7, residues with largest buried surface areas at the interface as assessed by PISA²⁸ include Q129, R131 and R136 that interact with the LRR domain of NLRP3 (Fig. 3b). R121, R131 and R136 also participate in hydrogen-bonding or charged interactions. NEK7 residues D261, E265 and E266 bury large surface areas at the interface with HD2 of NLRP3 (Fig. 3c, left). S260 and E266 also participate in hydrogen-bonding or charged interactions at this interface. For NBD interaction, NEK7 residues D290, K293, R294 appear to be the most extensive (Fig. 3c, right).

To deduce the importance of the observed contacts, we performed site-directed mutagenesis on NEK7 (Fig. 3d–e, Extended Data Fig. 6, 8c–e). Pulldown of SUMO-tagged wildtype (WT) and mutant NEK7 by MBP-tagged NLRP3 using amylose resin revealed that the most drastic effects came from mutations on Q129, R131 and R136 in the first half of the NEK7 C-lobe, all at the interface with the LRR of NLRP3 (interface I). The data explain the previous immunoprecipitation results in which a truncated NEK7 (aa1–212) removing the second half of the C-lobe supported NLRP3 binding¹³. The residues S260, D261 and E265 of NEK7 for HD2 interaction (interface II) also had substantial effects when mutated, whereas mutations on NEK7 residues for NBD interaction (interface III) did not cause notable changes in NLRP3 interaction (Fig. 3d–e, Extended Data Fig. 6, 8c–e). Collectively, the mutagenesis data support the importance of interfaces I and II in the NLRP3-NEK7 interaction. Of note, the NLRP3 NBD no longer contacts NEK7 in a model of active NLRP3 based on the active NLRC4 conformation^{19,20} (see below).

To further validate the observed NLRP3-NEK7 interface, we reconstituted WT and mutant NEK7 into NEK7^{KO} immortalized mouse bone marrow derived macrophages (iBMDMs) and examined the response of the cells upon LPS priming and nigericin treatment. While WT NEK7 rescued NEK7^{KO} iBMDMs in caspase-1 processing (Fig. 4a), IL-1 β secretion (Fig. 4b), and cell death (Extended Data Fig. 8f), the NEK7 mutants were compromised in supporting nigericin-induced NLRP3 activation (Fig. 4a–b, Extended Data Fig. 8f).

Specificity of NEK7 for NLRP3 and competition between NEK9 and NLRP3

NEK6 is a kinase closely related to NEK7 with an overall 87% sequence identity in the kinase domain (Extended Data Fig. 6), but it cannot support NLRP3 activation^{13,14}. Sequence comparison among NEKs suggests that the main determinant of the specificity

resides at the second part (residues 260–302) of the NEK7 C-lobe, while the first part (residues 120–259) of the NEK7 C-lobe is largely conserved with NEK6 (Extended Data Fig. 6). Because both NEKs are involved in mitosis through an interaction with NEK9, we mapped the NEK9-binding site onto the NEK7 structure from the crystal structure of a NEK7-NEK9 complex²⁹ (Extended Data Fig. 8g). Consistent with the sequence conservation, the NEK9-binding site is mainly formed by the first part of the NEK7 C-lobe (Extended Data Fig. 8g), and partially overlaps with the NLRP3-binding site of NEK7 (Extended Data Fig. 8h). In addition, the back-to-back homodimer of NEK7 in the NEK7-NEK9 crystal structure²⁹ postulated for trans-autophosphorylation is incompatible with NLRP3 interaction (Extended Data Fig. 8i). We hypothesize that once NEK7 binds NLRP3, it cannot be activated any more for mitosis. Hence, not only mitosis prevents NLRP3 inflammasome activation¹⁴, but NLRP3 inflammasome activation may also prevent mitosis, when NEK7 quantity in macrophages is limited¹⁴.

Structural insights into NLRP3 for NEK7 interaction

To test the functional relevance of NLRP3 residues contacting NEK7, we reconstituted WT and structure-based mutant NLRP3 into NLRP3^{KO} iBMDMs and examined the response to NLRP3 stimulation. Upon LPS priming and nigericin treatment, WT reconstitution of NLRP3^{KO} rescued processing of caspase-1 as dictated by the appearance of the p20 large subunit (Fig. 4c, Extended Data Fig. 7). The LRR mutants E800R, D748R and E743R were strongly defective in caspase-1 processing, whereas Y916G, E862R and V705R might be partially defective. The LRR mutant W831A had no discernible effect. A triple mutation in the HD2 region Q636R/E637R/E638R was strongly defective. In contrast, the Q357R mutant from the NBD is not defective. Similarly, nigericin-induced IL-1 β secretion and cell death showed a similar pattern of mutational effects (Fig. 4d, Extended Data Fig. 7, 8j), supporting that the LRR and HD2 domains, but not the NBD, are imperative for NEK7 interaction.

The importance of the LRR may explain why a partial LRR construct of NLRP3 (aa742–991) did not interact with NEK7¹³, while a more complete LRR domain construct (aa711–1033) interacted with NEK7 albeit with some affinity reduction as compared to the full-length NLRP3¹⁴. Consistently, NLRP3 phosphorylation at Y859 plays a negative regulatory role³⁰, as Y859 situates at the NEK7-binding site of LRR whose phosphorylation might cause steric hindrance and charge repulsion (Extended Data Fig. 8k). On the other hand, tyrosine phosphatase PTPN22 that dephosphorylates Y859 promotes NLRP3 activation and inflammatory bowel disease patients carrying an autoimmunity-associated allele of PTPN22 showed increased IL-1 β production³⁰. Although the NACHT domain also contacts NEK7, the ability of NACHT alone for NEK7 binding remains unresolved. In one study, an LRR deletion mutant (LRR, aa1–741) did not interact with NEK7¹³. In another study, LRR mutants (aa1–686, 1–695, 1–710, 1–720 and 1–731) interacted with NEK7 and reconstituted NLRP3^{-/-} macrophages for NLRP3 activation by multiple stimuli³¹. Intriguingly, constructs with less LRR truncations (aa1–850, 1–879, 1–907, 1–936, 1–965 and 1–996) were inactive in reconstituting NLRP3 activity³¹.

Modelled oligomeric assembly of the NLRP3-NEK7 complex

Previous studies on NLRC4 have shown that the NACHT domain undergoes a large rigid-body rotation at the HD1 to WHD junction to open up the structure for oligomerization and activation^{6,19,20,22,23}. We therefore modelled a hypothetical NLRP3 structure in an active conformation using the NLRC4 oligomer structure as a homology reference, which generates a $\sim 90^\circ$ rotation of the NBD-HD1 module (Fig. 5a). This modelling exercise placed the NBD-HD1-WHD module for direct interaction in the NLRP3 ring without steric hindrance (Fig. 5b). In contrast, the inactive conformation is not compatible with the modelled oligomeric structure (Fig. 5c). The modelling should not affect NEK7 binding because only the NBD-HD1 module is moved relative to NEK7 (Extended Data Fig. 8l, Supplementary Video 2) and the NBD contact is not essential for NEK7 interaction as shown by mutagenesis (Fig. 3d–e, 4c–d, Extended Data Fig. 8j).

Unexpectedly, modelling of the hypothetical NLRP3-NEK7 inflammasome disk based on the NLRC4 oligomer places NEK7 at the oligomerization interface (Fig. 5b, 5d, Extended Data Fig. 9a). In particular, residue E280 of NEK7 C-lobe opposite from its NLRP3-interacting surface contacts the neighbouring NLRP3 at residues S794, Q796 and K797 with a predicted buried surface area of 150 \AA^2 (Fig. 5d). To test the functional importance of these predicted interactions in the modelled NLRP3 oligomer, we reconstituted NEK7^{KO} or NLRP3^{KO} BMDMs using mutants on this new interface. As predicted, E280R or E280V did not affect its interaction with NLRP3 in a pulldown assay using recombinant proteins as E280 resides on the side of NEK7 opposite from its NLRP3-binding site (Fig. 3d–e). However, E280R did not rescue NLRP3 activation in NEK7^{KO} iBMDMs whereas WT NEK7 did (Fig. 4a–b). Within NLRP3, the double mutant S794A/Q796A and the triple mutant S794A/Q796A/K797A both failed to reconstitute NLRP3-induced caspase-1 processing and IL-1 β secretion in NLRP3^{KO} iBMDMs whereas WT NLRP3 did (Fig. 4c–d). To confirm that NLRP3 inflammasome assembly per se was disrupted by these mutations, we assessed NLRP3 inflammasome speck formation using immunofluorescence imaging. Indeed, while WT NEK7 and NLRP3 rescued speck formation in NEK7^{KO} or NLRP3^{KO} BMDMs, the NEK7 and NLRP3 mutants all failed to form speck in reconstituted iBMDMs upon nigericin stimulation (Extended Data Fig. 9b).

Interestingly, the NLRC4 inflammasome also has an additional oligomerization interface at the LRR (Extended Data Fig. 9c). Moreover, the recently identified NLRC4 autoinflammatory mutation W655C at this LRR-LRR interface (Extended Data Fig. 9d) promotes NLRC4 inflammasome assembly probably via enhancing the LRR-LRR interaction and causes the macrophage activation syndrome in human³². In NLRP3, the LRR itself is too short to reach the adjacent LRR in the hypothetical oligomer, and NEK7 bridges the gap between adjacent NLRP3 subunits. Collectively, these data support our model of NLRP3 activation and point to a previously unanticipated mechanism for the NEK7 requirement. In the modelled complex with the full-length NEK7, the NEK7 N-lobe projects away from the plane of the inflammasome ring and does not interfere with NLRP3 oligomerization (Fig. 5e).

NLRP3 CAPS mutations

To investigate the mechanism of autoinflammation in CAPS, we mapped the validated pathogenic mutations of NLRP3 on the Infevers website³³ to the structure (Fig. 6a, Extended Data Fig. 9e). These mutations are associated with Muckle-Wells syndrome (MWS), neonatal onset multisystem inflammatory disease (NOMID), or familial cold autoinflammatory syndrome (FCAS). Notably, almost all mutations lie in the NACHT domain and surround the ADP-binding site. One exception is G755 in the LRR near the NEK7-binding site, which exhibited enhanced interaction with NEK7 when mutated to Ala or Arg¹⁴.

Structural analysis suggests that the NACHT mutations may affect the inactive conformation and therefore enhance NLRP3 activation. These mutations may be categorized into three tiers: (1) those (R260, L264, D303, A352, T436, A439 and G569) at the inter-domain interfaces affecting with the important interactions stabilizing the inactive conformation; (2) those on the Walker B motif of the ATPase (D303 coordinating Mg²⁺ ions, and E304 for ATP hydrolysis³⁴); and (3) those (L305, T348, F523 and E627) buried within their respective domains, where mutations may affect the local domain conformation and indirectly destabilize the inter-domain interactions in the inactive state. For instance, while L305, T348 and F523 are uncharged, E627 forms a partially buried salt-bridge with R550 and K570 in the NLRP3 structure.

Concluding remarks

In summary, our structural and functional studies have demonstrated that the NLRP3-NEK7 interaction dictates the NEK7 requirement in NLRP3 inflammasome activation. We further show that the opposite side of NEK7, which is not required for initial NLRP3 interaction, is important for stimulus-dependent NLRP3 activation by bridging oligomerization. We propose that NLRP3 activation requires at least two steps (Fig. 6b). First, NLRP3 needs to be bound to NEK7, a process that is enhanced by priming and NLRP3 triggers^{13,14}. Second, formation of the NLRP3-NEK7 complex alone may not be sufficient to induce NLRP3 activation because NLRP3 oligomerization also requires the conversion of NACHT from an inactive to an active conformation. This conformational transition may require ATP binding and other unknown allosteric triggers, as NLRP3 has been shown to possess ATPase activity³⁴. In the NACHT domain-containing protein Apaf-1, binding of ATP or an ATP analogue, but not ATP hydrolysis, is required for Apaf-1 activation³⁵. The necessities of both NEK7 binding and the NACHT conformational change for NLRP3 activation are supported by the NEK7 requirement in macrophages containing the CAPS-associated R258W activating mutant of mouse NLRP3 (equivalent to R260W of human NLRP3) (Fig. 6a, Extended Data Fig. 9e) to activate caspase-1¹³. While NLRP3 activation is complicated by many factors including post-translational modifications³⁶⁻³⁹, our studies may have unravelled the intriguing mechanism for the NEK7-licensed NLRP3 inflammasome activation.

Our *in vitro* reconstituted NLRP3-NEK7 complex is clearly in an inactive state and we did not observe oligomers of the purified NLRP3-NEK7 heterodimer. ATP or ATP analogues,

which can induce conformational change and oligomerization of Apaf-1, did not induce oligomerization of the NLRP3-NEK7 heterodimer *in vitro*. We reasoned that this may be because NEK7 binding only licenses NLRP3, but is insufficient, for the inflammasome assembly. Despite extensive studies, the direct triggers for NLRP3 conformational change to mediate the inflammasome assembly are still unknown. In this regard, it is unclear whether one activated NLRP3-NEK7 complex will trigger a nucleated oligomerization similar to the PrgJ-NAIP2-NLRC4 inflammasome^{6,19,20} or the direct activator has to induce the conformational change of each NLRP3 molecule for inflammasome assembly. In plants, NLR-mediated effector-triggered immunity is often indirect in that multiple microbial effectors may first modify a common NLR-associated protein or a specific domain in an NLR, which then relays the invasion signal to the NLR for effector-triggered immunity⁴⁰. For NLRP3, it remains to be addressed whether NEK7 can be considered such a common sensor. These questions require further investigations.

Methods

Cloning, expression, purification and reconstitution of recombinant human NLRP3 and NEK7 complex.

Full-length (aa1–302) and N-terminally truncated (aa31–302) human NEK7 sequences were cloned into a modified pET28a vector with an N-terminal 6xHis-SUMO tag followed by the Ulp1-protease site. These constructs were transfected into *E. coli* BL21 (DE3) cells, which were grown in LB medium supplemented with 50 µg/ml kanamycin. Protein expression was induced overnight at 18 °C with 0.2 mM isopropyl-β-D-thiogalactopyranoside after optical density at 600 nm reached 0.8. For N-terminally truncated NEK7, cells were harvested and resuspended in a lysis buffer containing 20 mM Tris-HCl at pH 7.4, 300 mM NaCl, 0.5 mM Tris(2-carboxyethyl) phosphine hydrochloride (TCEP) and 20 mM imidazole. For the full-length NEK7, the lysis was performed in buffer containing 50 mM Tris-HCl at pH 7.5, 500 mM NaCl, 5 mM MgCl₂, 10 mM imidazole, 10% glycerol and 2 mM β-mercaptoethanol. The proteins were first purified by affinity chromatography using Ni-NTA beads (Qiagen). The 6xHis-SUMO tag was cleaved by overnight Ulp1 protease digestion with dialysis at 4 °C and removed by passing through Ni-NTA beads again. The NEK7 proteins with SUMO-tag or after protease cleavage were further purified by size exclusion chromatography on a Superdex 200 column (GE Healthcare Life Sciences) equilibrated with the gel filtration buffer containing 20 mM Tris-HCl at pH 7.5, 150 mM NaCl and 0.5 mM TCEP.

An artificial NEK7 dimer was engineered based on the PKR dimer structure (PDB ID: 2A19)¹⁸ by a back-to-back interaction at the N-terminal lobe. The N-terminal disordered region (residues 1–33) of NEK7 was replaced by the non-canonical helix α0 (residues 258–266) of PKR, and several surface residues at the predicted dimerization interface were mutated to corresponding residues in PKR (L54R, V58K, P59T, K87A, A99V, S100C, E103T and D104G). Protein expression and purification of the NEK7 dimer followed the same procedure as full-length or N-terminally truncated WT NEK7.

PYD-deleted NLRP3 (aa 134–1034) was cloned into a modified pFastBac vector with an N-terminal maltose-binding protein (MBP) tag. The sequence 134-YRKKYRK-140 was

changed to 134-YCAKYRA-140, designed to avoid a potential clash with the N-terminal MBP. The baculovirus of NLRP3 was prepared using the Bac-to-Bac® system (Invitrogen). To express the protein, 10 ml of the NLRP3 baculovirus was used to infect 1 litre Sf9 cells, which were harvested 48 hours post-infection. Cells were lysed by sonication in buffer containing 20 mM Tris-HCl at pH 7.5, 200 mM NaCl, 0.5 mM TCEP and 10% glycerol with freshly added protease inhibitor cocktail (Sigma). After centrifugation, the supernatant was incubated with 3 ml amylose resin at 4 °C for 1 hour. The mixture was then subjected to gravity flow and the bound MBP-tagged NLRP3 protein was eluted with 25 mM maltose. The eluted protein was further purified by size exclusion chromatography on a Superose 6 column (GE Healthcare Life Sciences) in the same gel filtration buffer used for NEK7.

The complexes of MBP-tagged NLRP3 with NEK7 monomer and dimer were reconstituted by size exclusion chromatography on a Superose 6 column equilibrated with the gel filtration buffer. The eluted proteins were analysed on SDS-PAGE gels for homogeneity and stoichiometry. The fractions were then pooled and concentrated for further analysis and cryo-EM data collection.

All mutagenesis experiments were performed by the QuikChange site-directed mutagenesis protocol using Q5 High-Fidelity 2X Master Mix (NEB). All plasmids were verified by DNA sequencing.

Microscale Thermophoresis (MST).

Proteins were labelled with the cysteine-reactive dye Alexa Fluor 488 C5 Maleimide (Thermo Fisher). Purified NLRP3 was incubated with ~20-fold molar excess of the dye in gel-filtration buffer for 1 hour. After labelling, the excess dye was removed by applying the sample on Superdex 200 column equilibrated with the gel filtration buffer. 0.05% Tween 20 was added in the protein buffer for MST measurements prior to the experiment.

Data sets were collected at a temperature of 25.1 °C. For Alexa488-labelled NLRP3 interaction with NEK7, a concentration series of NEK7 was prepared using a 1:1 serial dilution of NEK7 in gel filtration buffer supplemented with 0.05% Tween 20. The range of NEK7 concentration used was 32.5 µM to a final concentration of 1 nM over 16-serial diluted capillaries with 10 µl samples. The interaction was initiated by the addition 10 µl of 140 nM Alexa488-labelled NLRP3 to each reaction mixture resulting in a 70 nM final concentration of NLRP3. The LED power was 100% and the MST power (i.e. the power supplied to the infrared laser) was 60%. The pre-MST period was 5 s, the MST-acquisition period was 20 s, and the post-MST period was 5 s. Data was analysed by MO Control software provided by (NanoTemper, Munich, Germany). For analysis, the 32.5 µM concentration measurement was deleted as an outlier.

Multi-angle light scattering (MALS).

For molecular mass determination by MALS, protein samples were injected into a Superdex 200 (10/300 GL) gel filtration column equilibrated with the gel filtration buffer. The chromatography system was attached to a three-angle light scattering detector (miniDAWN TRISTAR) and a refractive index detector (Optilab DSP) (Wyatt Technology). Data were

collected every 0.5 s with a flow rate of 0.5 ml/min. Data analysis was carried out using ASTRA V.

Negative staining electron microscopy.

For negative staining, 4 μ l of an NLRP3-NEK7 complex was placed onto a glow-discharged copper grid (Electron Microscopy Sciences) coated with a layer of thin carbon, washed twice with H₂O, stained with 1–2% uranyl formate for 30 s and air-dried. The grids were imaged on a Tecnai G2 Spirit BioTWIN electron microscope and recorded with an AMT 2k CCD camera (Harvard Medical School Electron Microscopy Facility).

Cryo-EM data collection.

An NLRP3-NEK7 complex at 0.7 mg/ml was incubated with 0.3 mM ADP, 5 mM MgCl₂ and 0.3 mM MCC950 on ice for 30 min. A 3 μ l drop of the NLRP3-NEK7 complex was applied to a glow-discharged Quantifoil grid (R 1.2/1.3 400 mesh, copper, Electron Microscopy Sciences), blotted for 3–3.5 s in 100% humidity at 4 °C and plunged into liquid ethane using an FEI Vitrobot Mark IV. For data collection on an FEI Talos Arctica microscope operating at an acceleration voltage of 200 keV, movies were acquired on a K2 Summit direct electron detector (Gatan) in super-resolution counting mode, with 10.03 s total exposure time over 59 frames and an accumulated dose of 58.1 electrons per \AA^2 . The super-resolution pixel size was 0.5843 \AA . The defocus level in the data collection was set in the range of -1.0 to -3.0 μ m. A total of 3,667 movies were collected.

For data collection on an FEI Titan Krios G2 microscope operating at 300 keV, the cryo-grids were visually inspected for ice contaminations and flatness before loading into the microscope autoloader. Data collection utilized post-column BioQuantum energy filter (Gatan) in zero-loss imaging mode with a 20 μ m energy slit and K2 Summit direct electron detector (Gatan) in super-resolution counting mode (Peking University Electron Microscopy Laboratory and Cryo-EM Platform). Although the grids appeared to have icy areas, there were plenty of good holes, yielding images that were free of strong diffraction patterns corresponding to crystalline ice. Coma-free alignment was manually optimized before data collection; the parallel-beam illumination area under a nanoprobe mode was selected to achieve the optimal dose rate, avoid exposure interference and minimize edge fringes on the image. To increase collection efficiency, the data were collected in part with multiple exposures per grid hole, during which the image shift applied was no more than 250 nm. The data collection process was setup and carried out in SerialEM⁴¹. Movies were acquired with a dose rate of 5.4 electrons/s per physical pixel, and a total dose of 54.8 electrons per \AA^2 equally distributed in 7.2 s to 40 frames. The super-resolution pixel size was 0.42 \AA . A total of 15,861 movies were collected during 5 separate sessions, among which 1,340 movies were collected with a moderate stage tilt of 20°. The defocus levels of the images were set in the range of -0.8 to -3.0 μ m.

Cryo-EM data processing.

For Arctica data processing, raw movies were corrected by gain reference and for beam-induced motion, and summed into motion-corrected images using MotionCor2⁴². The CTFFIND4 program⁴³ was used to determine the actual defocus level of each micrograph.

RELION 3.0⁴⁴ and cisTEM⁴⁵ were used for subsequent image processing (Extended Data Fig. 2). First, template-free autopicking was used to generate an initial particle set for 2D classification. Good 2D classes were then used as templates for additional autopicking. Almost 1 million particles were picked which were subjected to multiple rounds of 2D classification until the classes looked homogenous. A few good class averages in different orientations were selected for the reconstruction of an initial model, which was low-pass filtered to 60.0 Å to use as the input reference for 3D classification of 522,320 particles. One selected 3D class was further classified and refined to reach an overall resolution of 4.3 Å measured by gold-standard Fourier shell correlation (FSC) between half maps (Extended Data Table 1). Due to particle orientation preference, the map suffers from anisotropic resolution.

Krios data processing also used MotionCor2⁴² for aligning and summing movie frames at the pixel size 0.84 Å. The averaged images were binned 3-fold to obtain TIFF images for visual screening. Bad images such as those with excessive ice contaminants were removed. The CTF parameters of each drift-corrected micrograph were then calculated using the program Gctf⁴⁶. Particles were automatically picked from 2-fold binned micrographs using Gautomatch (<https://sbgrid.org/software/titles/gautomatch>) and a Gaussian sphere template, which yielded a total of 1,850,332 particles. Reference-free 2D and 3D classifications were carried out with both Relion 3.0⁴⁴ and ROME 1.1.2⁴⁷. The latter combines maximum-likelihood based image alignment with statistical machine-learning based classification⁴⁷, and could output a large number of refined 2D classes with subtle differences. The NLRP3-NEK7 complex particles naturally and preferentially orientated with the curved LRR plane on the grid plane. To alleviate this orientation preference, we first included a subset of data that were collected with a modest 20° stage tilt. Because of the large vertical drift of carbon grids projected in the lateral direction, we could not use a larger tilt. We also retained as many particles as possible from the rare views that may not have been previously included in Relion-based 2D classification. This was done by multiple rounds of deep unsupervised 2D classifications with the ROME 1.1.2 package⁴⁷, which allowed us to improve the conformational homogeneity of selected particles. 3D classification and refinement were carried out in Relion 3.0⁴⁴. Map reconstruction was done with ROME 1.1.2⁴⁷, and local resolution map was produced with ResMap⁴⁸ that is embedded in Relion 3.0⁴⁴ (Extended Data Fig. 3). Inclusion of the tilted data and deep 2D classification spread out the orientation distribution and helped to improve the overall features, such as the connecting loop density on both sides of the LRR region. Data processing statistics is summarized (Extended Data Table 1).

Model building and display.

NLRP3 initial homology model was generated using the Phyre2 server²⁴. Manual adjustment, rigid-body fitting, flexible fitting and segment-based real-space refinement were performed in distinct parts of the initial model to fit in the density in Coot⁴⁹, with help of Chimera⁵⁰ and real space refinement in Phenix⁵¹. In the fitting to the final 3.8 Å map, large side-chain densities were used to guide the local register of the backbone trace. For example, W774 and W831 flanking the inner surface of the LRR domain were used to confirm the residue register in LRR. The density observed accounts for NLRP3 residues (aa133–1034)

that include NBD, HD1, WHD, HD2 and LRR domains. A few unstructured regions including part of the HD2 domain (aa654–683) were omitted due to poor density. The model was fitted and modelled to the best of our knowledge. The remaining part of the cryo-EM map was fitted with the NEK7 crystal structure (2WQN)²⁵. Only NEK7 C-terminal lobe residues (aa113–300) were fitted in the density because the N-lobe density appeared to have been averaged out in the data processing, likely due to flexibility. Interaction analysis was conducted using PISA²⁸ and structure representations were generated in Chimera⁵⁰, Pymol⁵² and ResMap⁴⁸.

Thermal shift assay.

Purified 2 μ M NLRP3 or NEK7 was mixed with 1-fold protein thermal shift dye (Thermo fisher scientific) and 200 μ M MCC950 or ADP or 100 μ M MCC950 plus 100 μ M ADP in a 20 μ l reaction volume. Thermal scanning (25 to 75 $^{\circ}$ C at 1.5 $^{\circ}$ C/min) was performed and melting curves were recorded on a StepOne RT-PCR machine. Data analysis was done by Protein Thermal ShiftTM Software (Thermo Fisher Scientific).

In vitro pull-downs.

1.5 μ M MBP-tagged NLRP3 was mixed with 3 μ M full-length WT or mutant NEK7 in buffer containing 30 mM HEPES at pH 7.5, 150 mM NaCl and 0.5 mM TCEP, and incubated for 1 h on ice. The mixture was further incubated for 1 h with 30 μ l amylose resin and washed twice with 250 μ l of the same buffer followed by 1 h elution with 50 mM maltose. Input and elution fractions were analysed with SDS-PAGE. NEK7 and NLRP3 bands were quantified with ImageJ and efficiency of binding was calculated from the ratio of NEK7 to NLRP3 band intensities. Three independent experiments were performed, and the efficiency of binding was presented as mean \pm standard deviation.

Generation of stable cell lines and cellular reconstitution.

To reconstitute NLRP3^{KO} iBMDMs with WT or mutant full-length mNeonGreen (mNG)-tagged human NLRP3, lentiviral particles were generated as follows. On day 0, the lentivirus was produced using HEK293T (60% confluent) cells by co-transfecting 1 μ g of a pLV vector containing the WT or mutant NLRP3, 750 ng psPAX2 packaging plasmid, and 250 ng pMD2.G envelope plasmid. The packaging and envelope plasmids were gifts from Didier Trono (Addgene no: 12260 and 12259, respectively). The transfected cells were incubated overnight. On day 1, the media were removed, and replenished with 1 ml fresh medium. The cells were incubated for another day. The expression was analysed by a confocal laser scanning microscope FluoView FV1000 (Olympus America, Waltham, MA), equipped with 488 Argon for green excitation.

On day 2, the supernatant containing the virus was filtered using a 0.45 μ m filter and used directly to infect NLRP3^{KO} iBMDMs (2.5×10^6 cells/ml) using a spinfection protocol to increase the efficacy. Spinfection was performed at $2,500 \times g$ for 90 minutes at 37 $^{\circ}$ C using 8 μ g/ml polybrene (Santa Cruz Biotechnology, Cat. no: sc-134220). Post spinfection, cells were further incubated for the expression of reconstituted proteins for 48 hours. Reconstitution was verified by western blotting using a specific anti-human NLRP3 antibody (Adipogen, Cat no: AG-20B-0014-C100).

Inflammasome activation assays.

NLRP3^{KO} iBMDMs reconstituted with human WT or mutant NLRP3 were seeded at a density of 3×10^6 cells/ml. On the next day, the cells were primed with 1 μ g/ml *lipopolysaccharides* (LPS) (Invivogen, Cat. no: tlr-b5lps) for 4 hours. Post priming, the cells were activated with 20 μ M nigericin (Sigma-Aldrich, Cat. no: N7143-5MG) for 30 minutes, and the supernatant was collected. Released IL-1 β was analysed using an ELISA kit (Affymetrix eBioscience, Cat. no: 88-7013), and released LDH was measured using the LDH Glo™ cytotoxicity assay (Promega, Cat. no: J2380), according to manufacturer's instructions. For analysis of caspase-1 cleavage, the whole cell lysate was prepared in 1X laemmli sample buffer, resolved on 12.5% SDS-PAGE and Western blotted using a specific anti-mouse caspase-1 antibody (Adipogen, Cat. no: AG-20B-0042-C100). The graphs were plotted using GraphPad prism 7 software.

Immunolabeling and antibodies.

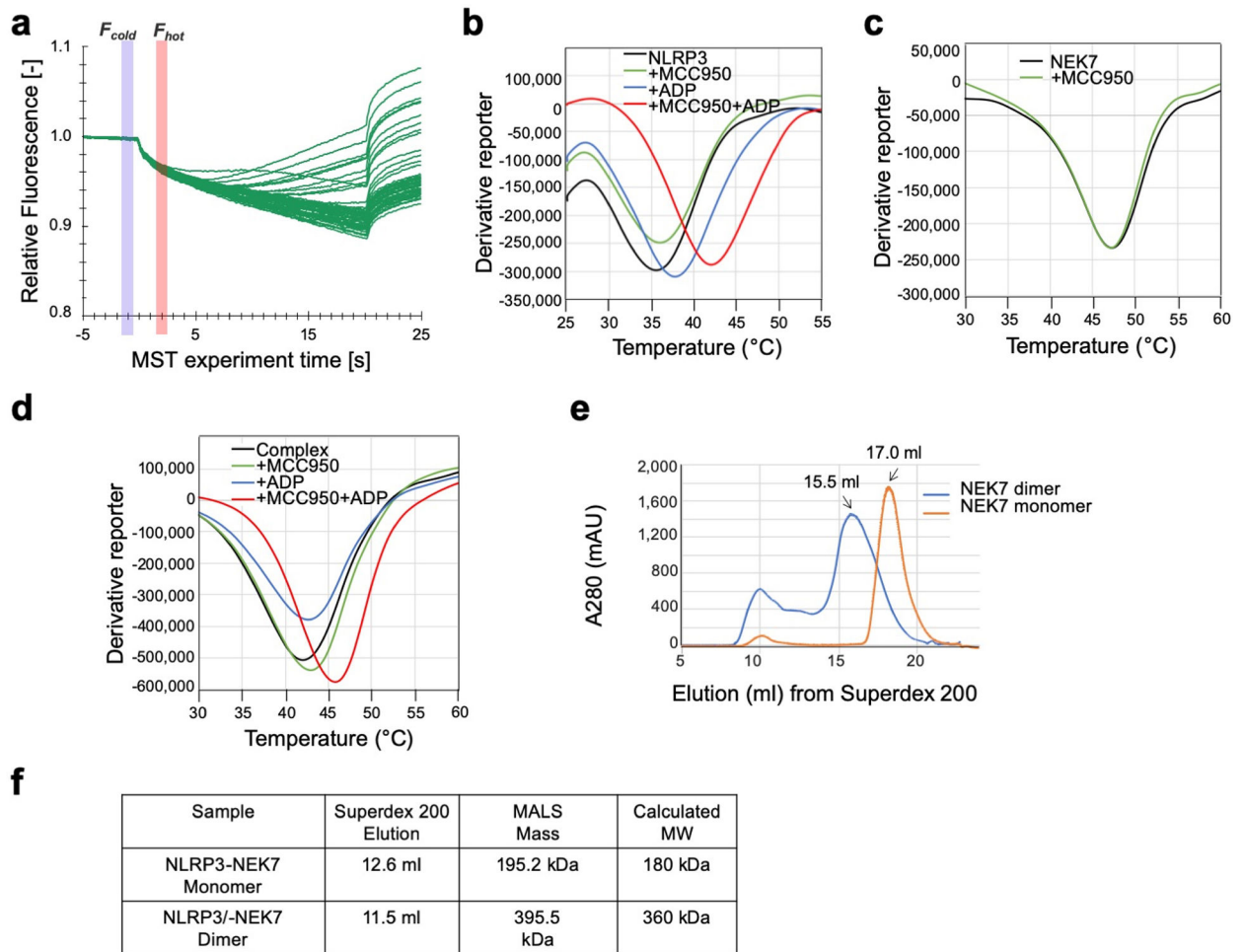
Reconstituted iBMDM cells were primed for 4 hours with LPS, and then activated with nigericin for 30 minutes. Fixative, permeabilization, and blocking buffers were prepared in Brinkley Buffer 80 (BRB80), and kept at 37 °C prior to use. BRB80 buffer was prepared freshly using 80 mM PIPES, 1 mM MgCl₂, 1 mM EGTA, titrated to pH 6.8 with saturated solution of KOH.

Cells were fixed in 3.7% paraformaldehyde for 5 minutes at room temperature. Afterwards, cells were washed twice using BRB80 with 5 minutes interval between washes. Permeabilization was carried out for 5 minutes at room temperature using 0.15% Triton X-100 (in 1X BRB80). Washing was carried out to remove permeabilization buffer. Cells were then blocked for 1 hour at room temperature using blocking buffer (3% gelatin from cold water fish skin prepared in 1X BRB80). Cells were incubated with primary antibody for overnight (anti-ASC, 1:1,000, Cell Signaling Technology, Cat. no: 67824S). The cells were washed and incubated with secondary antibody for an hour at room temperature (Goat anti-rabbit (H+L), Alexa Fluor 647 HRP conjugated 1:10,000, Thermo Fischer Scientific, Cat. no: A-21245). Nucleus was stained using Hoechst 33342 (Invitrogen, Cat. no: H3750). In between, extensive washing steps were carried out to remove unbound antibodies and stains.

Confocal laser scanning microscopy.

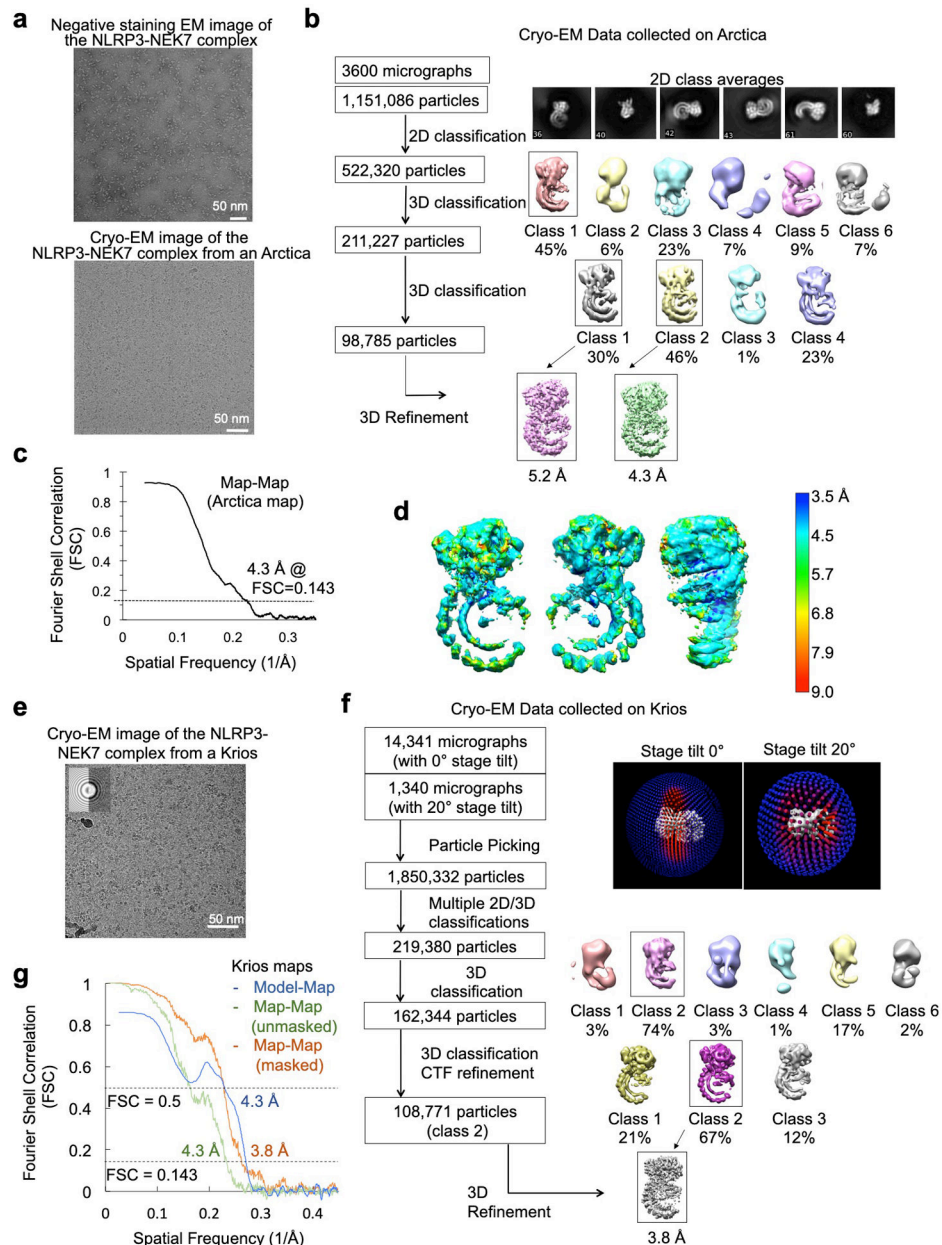
Reconstituted iBMDMs, post-activation, were washed once with 1X BRB buffer, fixed and labelled with antibodies as mentioned in immunolabeling and antibodies section. Confocal sections were obtained with an Olympus confocal laser scanning microscope FluoView FV1000 (Olympus America, Waltham, MA), equipped with 405 Diode (for blue excitation), 635 diode (for far red excitation). Images were captured using 40x (0.95 NA, air objective), with Olympus FluoView version 3.0 viewer software. The images were identically acquired, and processed using Adobe Photoshop software.

Extended Data



Extended Data Fig. 1 | NLRP3-NEK7 protein purification and characterization.

a, Raw traces (of three independent replicates) of MST measurements corresponding to titration of NEK7 against Alexa488-labelled NLRP3. **b-d**, Representative thermal denaturation curves of NLRP3 (**b**), NEK7 (**c**) and complex (**d**), alone and in the presence of ADP and/or MCC950. The peak minima of the derivative curves correspond to the protein melting temperatures (T_m) (repeated 3 times). **e**, Gel filtration profile of WT NEK7 (monomer) and engineered NEK7 dimer on Superdex 200 column (repeated 5 times). **f**, Molecular masses of NLRP3-NEK7 dimer and monomer complexes measured by in-line multi-angle light scattering (MALS).



Extended Data Fig. 2 | Analysis and work flow for cryo-EM data collected on a Talos Arctica and on a Titan Krios.

a A negative staining EM image (top, one among a few hundred images) and a cryo-EM micrograph (bottom, one among a few thousand images) of the NLRP3-NEK7 complex from a Talos Arctica. Scale bars equal 50 nm. **b**, Work flow of cryo-EM data analysis of the Arctica data performed in Relion 3.0⁵³ and cisTEM⁴⁵. **c**, Gold-standard FSC curve between two half maps from the Arctica data. **d**, Local resolution estimation of the Arctica map generated by ResMap⁴⁸, coloured on the cryo-EM density (8σ). Highest resolution is observed where NEK7 interacts with NLRP3. **e**, A cryo-EM micrograph of the NLRP3-NEK7 complex from a Titan Krios (one among a few thousand images). Scale bar in the micrograph is 50 nm. The inset shows the modelled (left) and actual (right) Thon rings. **f**,

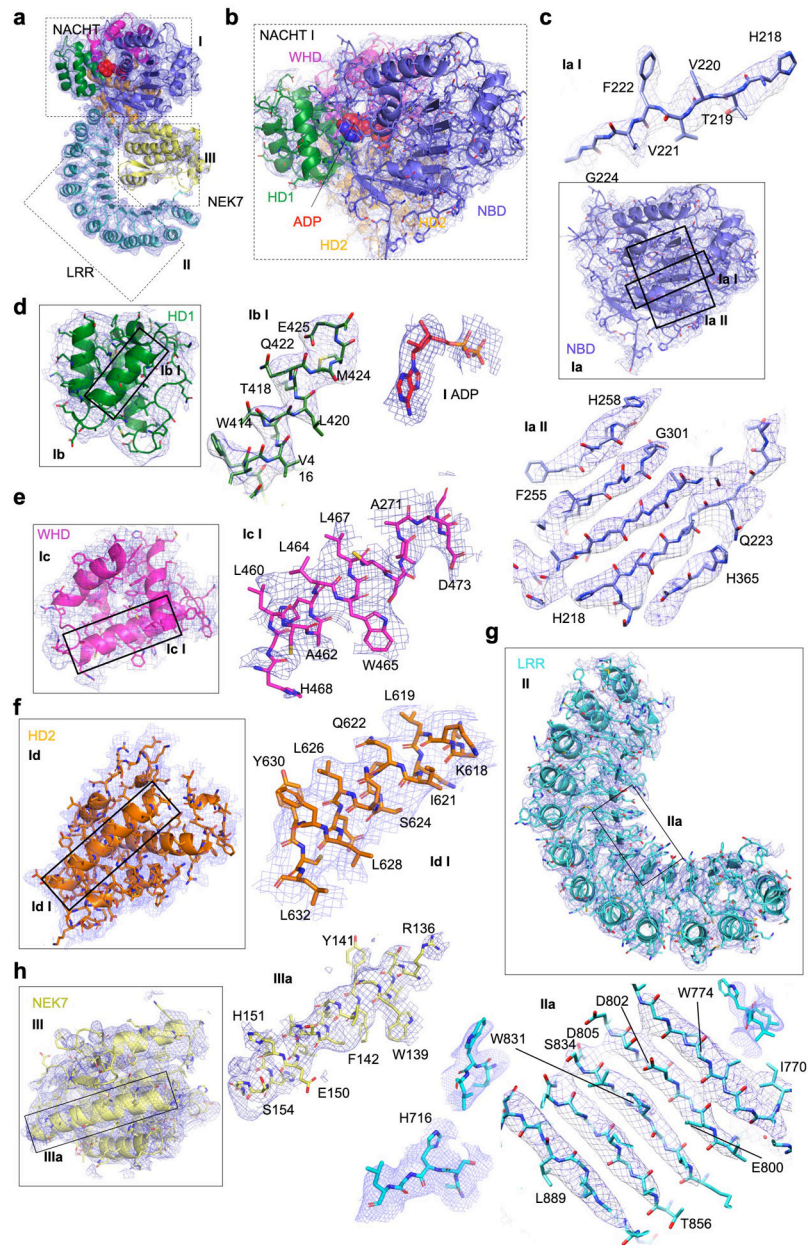
Work flow of cryo-EM data analysis of the Krios data done in Relion 3.0⁵³ and ROME1.1⁴⁷. The upper right insets show the orientation distributions of the particles from the dataset of tilt 0° and tilt 20° respectively. **g**, Gold-standard FSC curves between two half maps from the Krios data with mask (orange) and without mask (green), and between map and model (blue).

Author Manuscript

Author Manuscript

Author Manuscript

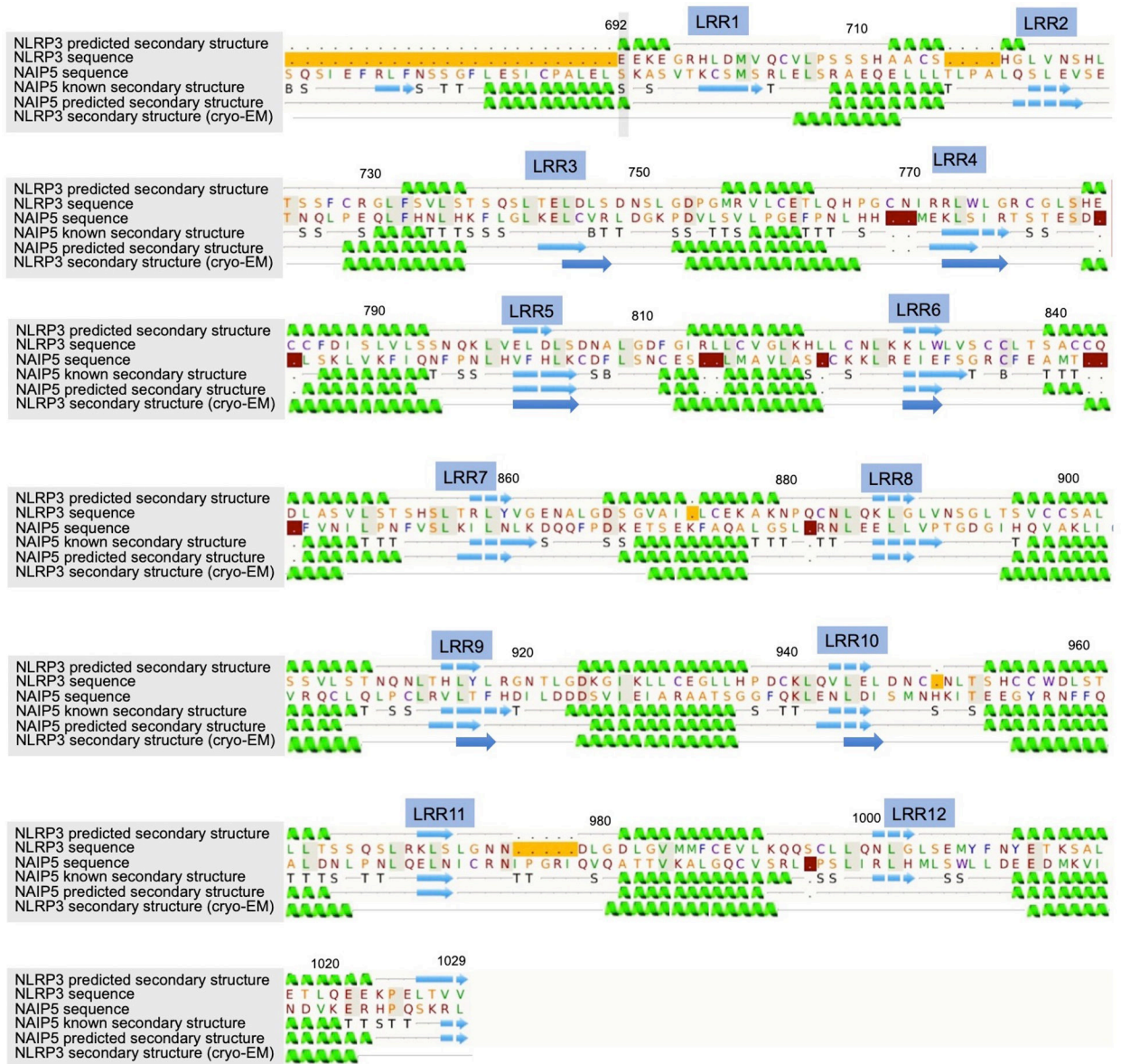
Author Manuscript



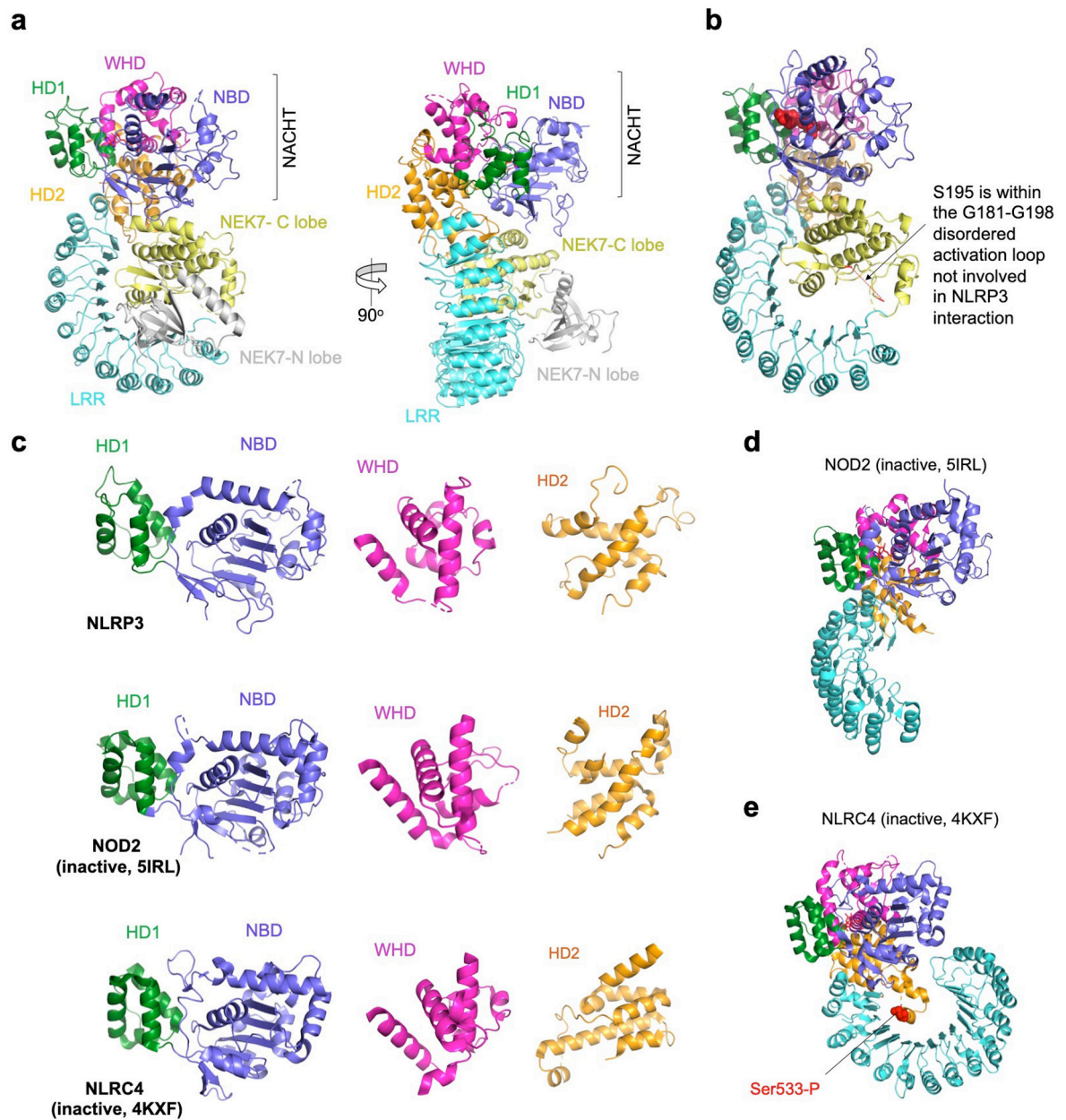
Extended Data Fig. 3 | Local density fitted with NLRP3 and NEK7.

All zoom-in views are labelled with domain names and selected segment residue numbers.

Densities are shown at 3σ .

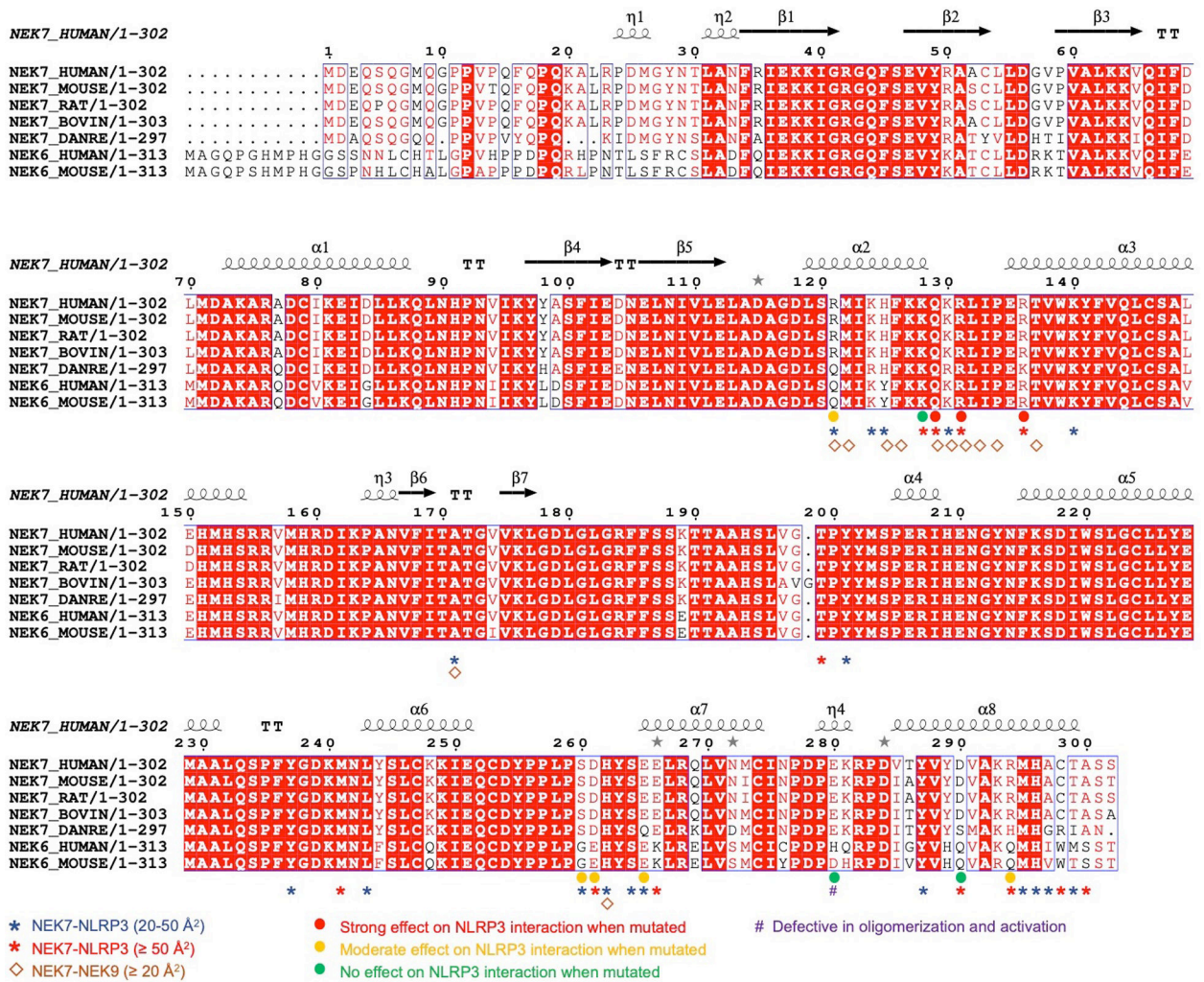


Extended Data Fig. 4 | Predicted and cryo-EM-derived secondary structures of the NLRP3-LRR domains aligned to NLRP3 and NAIP5 sequences.
 12 LRRs in NLRP3 were predicted by the Phyre2 server²⁴.

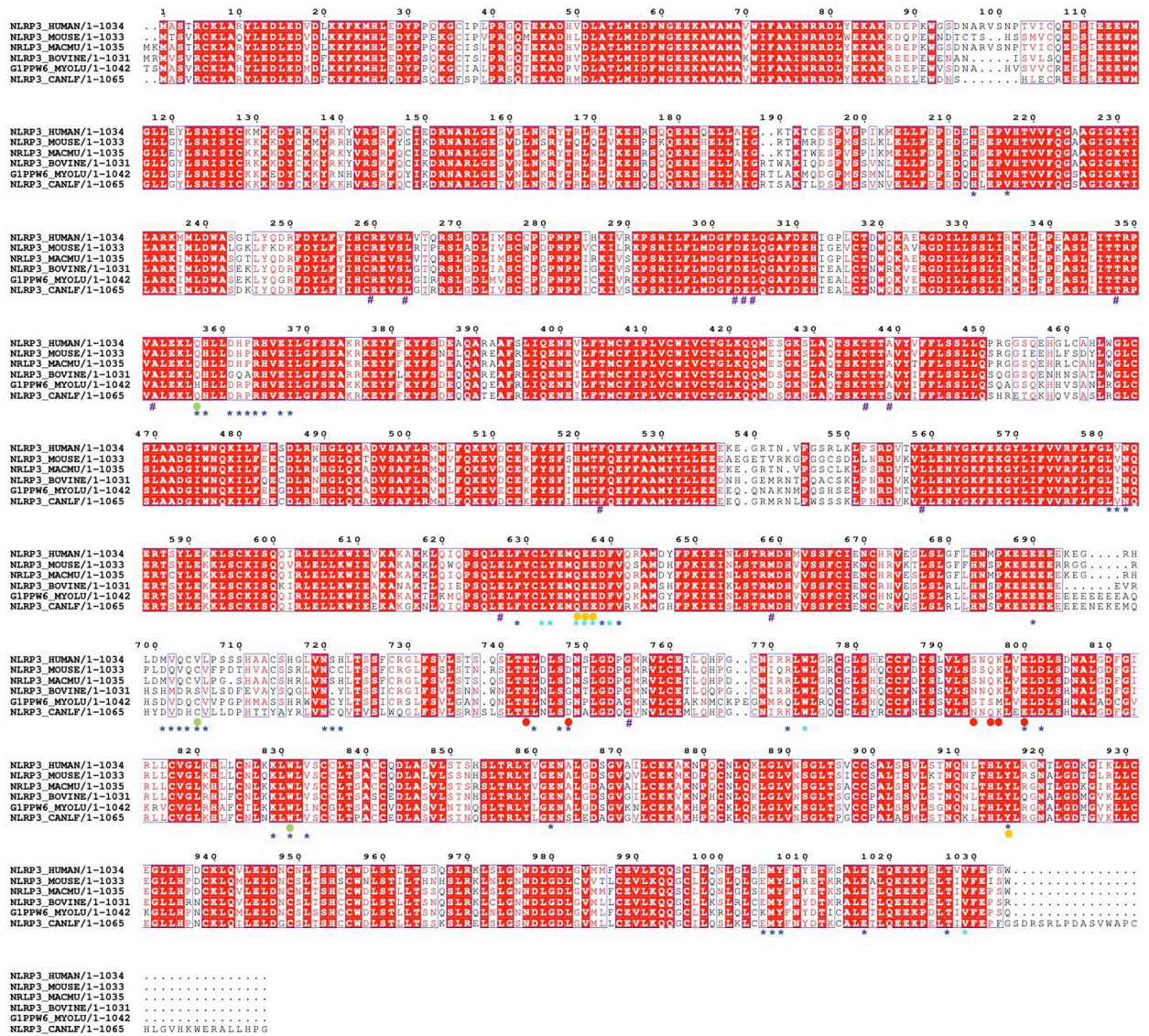


Extended Data Fig. 5 | The NLRP3-NEK7 complex structure showing the modelled full length NEK7 and NLRP3 domain comparisons.

a, Two views of the NLRP3-NEK7 complex structure with the NEK7-N lobe (gray) modelled from the NEK7 crystal structure (2WQM). **b**, The disordered activation loop including S195 in the NLRP3-NEK7 complex, which is not involved in NLRP3 interaction. **c**, NBD-HD1, WHD and HD2 of NLRP3, NOD2 (5IRL) and NLRC4 (4KXF) superimposed and shown side by side for comparison. **d-e**, NOD2 (d) and NLRC4 (e) structures^{6,21} in inactive conformations and in the orientation of NLRP3 (a) by superposing on the NBD-HD1 domains. Location of phosphorylated Ser533 of NLRC4 is labeled.



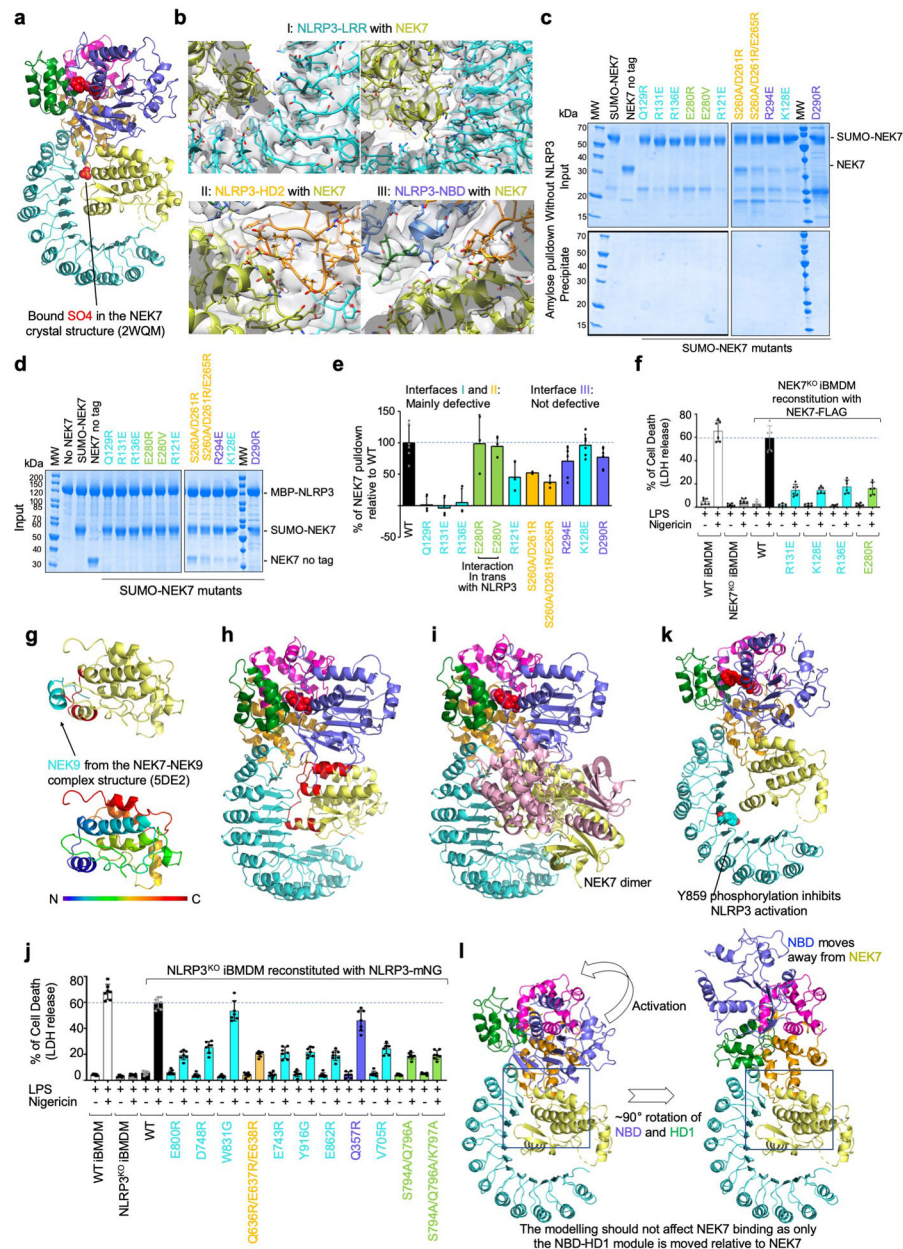
Extended Data Fig. 6 |. Multiple sequence alignment of NEK7 and NEK6.
 Multiple sequence alignment was performed by the eScript server⁵⁴. Annotations are based on the PISA server²⁸ analysis and mutational data from Fig. 3 and Fig. 4.



- * Buries 20-50 Å surface area
- * Buries ≥ 50 Å surface area
- Strong effect on NEK7 interaction when mutated
- Moderate effect on NEK7 interaction when mutated
- No effect in NEK7 interaction when mutated
- # CAPS mutations (inFevrs site)

Extended Data Fig. 7 | Multiple sequence alignment of NLRP3.

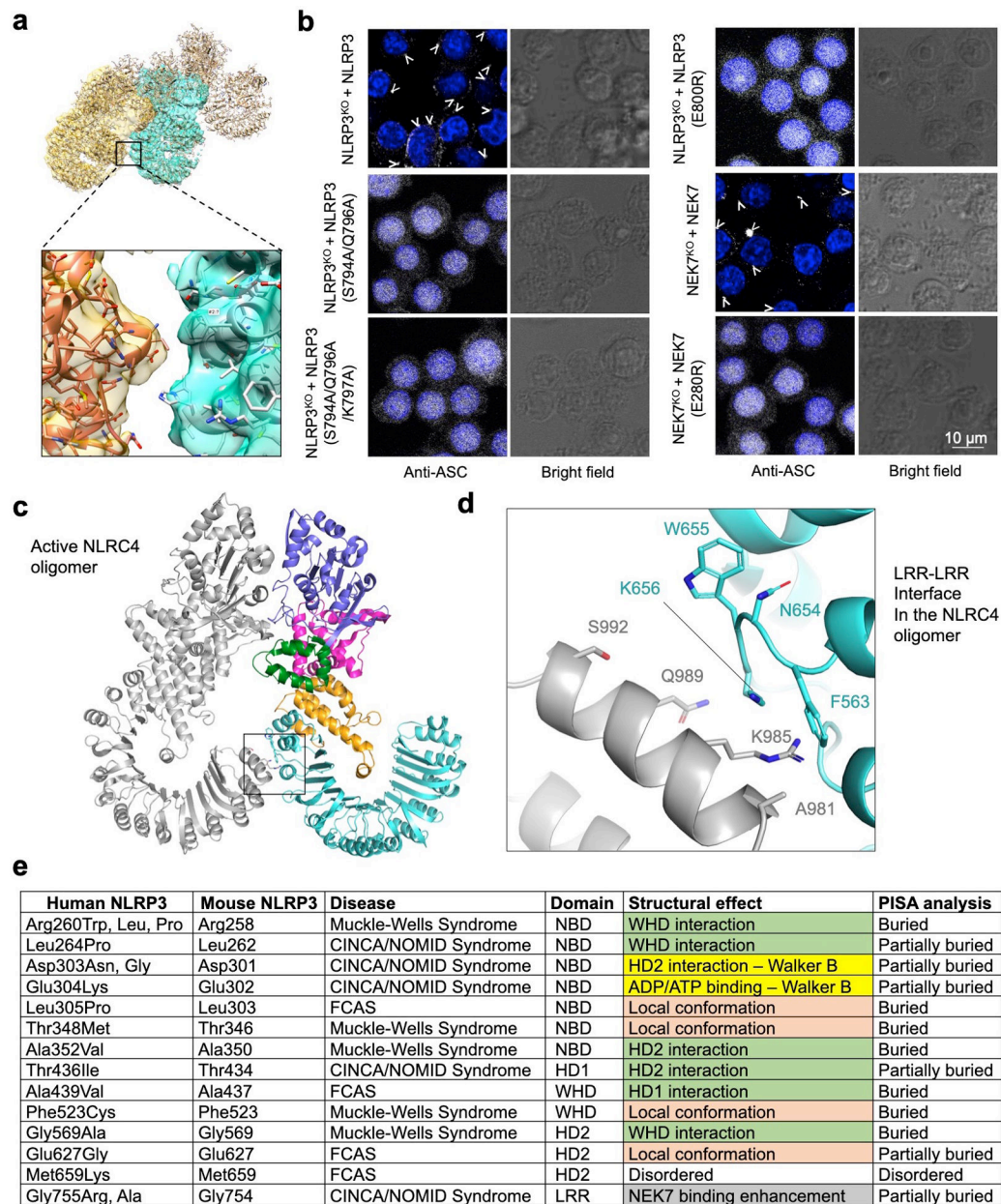
Multiple sequence alignment was performed by the eScript server⁵⁴. Annotations are based on the PISA server²⁸ analysis and mutational data from Fig. 3 and Fig. 4.



Extended Data Fig. 8 | Structural analysis, mutagenesis tests and overlap between the NEK9- and NLRP3-binding sites on NEK7.

a, Position of the bound SO_4 ion as in the NEK7 crystal structure²⁵, superimposed here in the NLRP3-NEK7 complex structure. **b**, Cryo-EM densities (5σ) at the NLRP3-NEK7 interfaces. Views correspond to those of Fig. 3b–c. **c**, Amylose pull-down of WT and mutant NEK7 without NLRP3, showing input and precipitate gels, which serve as negative controls for Fig. 3d. Experiments were repeated 3–6 times. **d**, Input gel for amylose pull-down of WT and mutant NEK7 shown in Fig. 3d. Experiments were repeated 3–6 times. **e**, Alternative calculation of the % of NEK7 pull-down relative to WT by subtracting the NEK7/NLRP3 ratio in the absence of NEK7 from the observed NEK7/NLRP3 ratio (shown as mean \pm s.d. for $n=3-6$) **f**, Cytoplasmic LDH released into the supernatant quantified by comparison with

total intracellular LDH of untreated cells (Triton X-lysed). Data are presented as mean \pm s.d. for n=3 from two independent experiments. **g**, Top: Mapping the NEK9-binding site onto the NEK7-NEK9 complex structure (5DE2)²⁹. NEK7 and NEK9 are shown in yellow and cyan, respectively, with the NEK9-binding residues of NEK7 highlighted in red. Bottom: A rainbow coloured NEK7 structure showing that the NEK9-binding residues are from the first part of the NEK7 C-lobe. **h**, Mapping the NLRP3-binding site (red) onto NEK7 in the NLRP3-NEK7 structure. The NLRP3-binding site overlaps with the NEK9-binding site on NEK7. **i**, Superposition of NEK7 back-to-back dimer (yellow and pink) in the NEK7-NEK9 complex structure (5DE2)²⁹ onto the NEK7 monomer in the NLRP3-NEK7 structure. The pink monomer in the NEK7 dimer clashes with NLRP3, suggesting that NEK7 dimerization cannot occur in the NLRP3-NEK7 complex. **j**, NLRP3^{KO} iBMDMs were reconstituted with WT or mutant human mNeonGreen-tagged NLRP3, primed by LPS (4 hours) and stimulated by nigericin (30 min). LDH release were analysed as in Extended Data Fig. 8f. Dots: individual data points. Data are presented as mean \pm s.d. for n=3 from two independent experiments. **k**, LRR phosphorylation at Y859³⁰ that might cause steric and charge repulsion with NEK7. **l**, NLRP3 activation model and NEK7 interactions. The hypothetical $\sim 90^\circ$ rotation of NBD-HD1 of NLRP3 upon activation moves NBD away from the NEK7 interaction region indicated by a box.



Extended Data Fig. 9 |. NLRP3-NEK7 interaction in trans and NLRP3 CAPS mutations.

a, Cryo-EM density (5σ) fitted to the oligomeric model, zoomed in at an NLRP3-NEK7 interface in trans. **b**, Immunofluorescence imaging for assessing ASC speck formation. NLRP3^{KO} and NEK7^{KO} iBMDMs were reconstituted with WT and mutant constructs as depicted. ASC speck formation upon nigericin activation was analysed by anti-ASC antibody. Nucleus was stained by Hoechst 33342. Scale bar 10 μ m. Images are representative of two independent experiments **c**, An active NLRC4 oligomer structure²⁰ shown for the LRR-LRR interaction. **d**, Zoom-in view showing the detailed LRR-LRR interaction in trans boxed in (c). **e**, Mapping of pathogenic disease mutations onto the NLRP3 structure. CAPS-associated pathogenic mutations derived from the Infevers database³³ are shown with predicted effect based on the NLRP3 structure. Green: disruption

of inter-domain interactions in the inactive conformation; mauve: change of local conformation by mutating residues buried within the domains; yellow: alteration in key residues in the Walker B motif; grey: enhancement of NEK7 binding.

Extended Data Table 1.

Cryo-EM data collection, refinement and validation statistics

	NLRP3-NEK7 Talos Arctica dataset	NLRP3-NEK7 Titan Krios dataset
Data collection and processing		
Magnification	105,000	165,000
Voltage (keV)	200	300
Electron exposure (e-/Å ²)	~59	~55
Defocus range (μm)	-0.5 to -3.0	-0.8 to -3.0
Super Resolution pixel size (Å)	0.589	0.42
Symmetry imposed	C1	C1
Initial particle images (no.)	1,086,055	1,850,332
Final particle images (no.)	98,340	108,771
Map resolution (Å)	4.3	3.8
FSC threshold	0.143	0.143
Map resolution range (Å)	3.5-5.8	2.5-6.6
Refinement		
Initial model used		
Model resolution (Å)		4.3
FSC threshold		0.5
Model resolution range (Å)		2.5-6.6
Map sharpening <i>B</i> factor (Å ²)		-100
Model composition		
Non-hydrogen atoms		7979
Protein residues		980
Ligands		1
<i>B</i> factors (Å ²)		
Protein		132.7
Ligand		96.7
R.m.s. deviations		
Bond lengths (Å)		0.006
Bond angles (°)		1.345
Validation		
MolProbity score		2.35
Clashscore		8.92
Poor rotamers (%)		1.91
Ramachandran plot		
Favoured (%)		84.96
Allowed (%)		14.02
Disallowed (%)		1.02

Supplementary Material

Refer to Web version on PubMed Central for supplementary material.

Acknowledgements

We thank the University of Massachusetts Cryo-EM Core Facility and the National Cryo-EM Facility at the National Cancer Institute for 200 keV data collection, the Electron Microscopy Laboratory and Cryo-EM Platform at Peking University for 300 keV data collection, and C. Xu, K. Song, K. Lee, X. Li, Y. Ma and D. Yu for technical support. This work was funded in part by the US NIH grant DP1HD087988 (H.W.), R01AI124491 (H.W.), R01AI06331 (G.N.), an Intel Corporation academic grant (Y.M.), the Thousand Talents Plan of China (Y.M.), National Natural Science Foundation of China grant 11774012 (Y.M.), and Natural Science Foundation of Beijing City grant Z180016 (Y.M.). Data processing was performed in part in the Sullivan cluster, which is funded in part by a gift from Mr. and Mrs. Daniel J. Sullivan, Jr., and in the Weiming No.1 and Life Science No. 1 High-Performance Computing Platform at Peking University. We thank Harry Leung (PCMM, BCH confocal core facility manager).

References

1. Lamkanfi M & Dixit VM Mechanisms and functions of inflammasomes. *Cell* 157, 1013–1022 (2014). [PubMed: 24855941]
2. Broz P & Dixit VM Inflammasomes: mechanism of assembly, regulation and signalling. *Nat Rev Immunol* 16, 407–420 (2016). [PubMed: 27291964]
3. Guo H, Callaway JB & Ting JP Inflammasomes: mechanism of action, role in disease, and therapeutics. *Nat Med* 21, 677–687 (2015). [PubMed: 26121197]
4. Shi J, Gao W & Shao F Pyroptosis: Gasdermin-Mediated Programmed Necrotic Cell Death. *Trends Biochem Sci* (2016).
5. Liu X et al. Inflammasome-activated gasdermin D causes pyroptosis by forming membrane pores. *Nature* 535, 153–158 (2016). [PubMed: 27383986]
6. Hu Z et al. Crystal structure of NLRP4 reveals its autoinhibition mechanism. *Science* 341, 172–175 (2013). [PubMed: 23765277]
7. Lu A et al. Unified polymerization mechanism for the assembly of ASC-dependent inflammasomes. *Cell* 156, 1193–1206 (2014). [PubMed: 24630722]
8. Lu A et al. Molecular basis of caspase-1 polymerization and its inhibition by a new capping mechanism. *Nat Struct Mol Biol* 23, 416–425 (2016). [PubMed: 27043298]
9. Lu A et al. Plasticity in PYD assembly revealed by cryo-EM structure of the PYD filament of AIM2. *Cell Discovery* 1, 15013 (2015). [PubMed: 26583071]
10. Rathinam VA, Vanaja SK & Fitzgerald KA Regulation of inflammasome signaling. *Nat Immunol* 13, 333–332 (2012). [PubMed: 22430786]
11. Munoz-Planillo R et al. K(+) Efflux Is the Common Trigger of NLRP3 Inflammasome Activation by Bacterial Toxins and Particulate Matter. *Immunity* 38, 1142–1153 (2013). [PubMed: 23809161]
12. Chen J & Chen ZJ PtdIns4P on dispersed trans-Golgi network mediates NLRP3 inflammasome activation. *Nature* 564, 71–76 (2018). [PubMed: 30487600]
13. He Y, Zeng MY, Yang D, Motro B & Nunez G NEK7 is an essential mediator of NLRP3 activation downstream of potassium efflux. *Nature* (2016).
14. Shi H et al. NLRP3 activation and mitosis are mutually exclusive events coordinated by NEK7, a new inflammasome component. *Nat Immunol* 17, 250–258 (2016). [PubMed: 26642356]
15. Schmid-Burgk JL et al. A Genome-wide CRISPR (Clustered Regularly Interspaced Short Palindromic Repeats) Screen Identifies NEK7 as an Essential Component of NLRP3 Inflammasome Activation. *J Biol Chem* 291, 103–109 (2016). [PubMed: 26553871]
16. Shi H, Murray A & Beutler B Reconstruction of the Mouse Inflammasome System in HEK293T Cells. *Bio Protoc* 6 (2016).
17. Coll RC et al. A small-molecule inhibitor of the NLRP3 inflammasome for the treatment of inflammatory diseases. *Nat Med* 21, 248–255 (2015). [PubMed: 25686105]

18. Dar AC, Dever TE & Sicheri F Higher-order substrate recognition of eIF2 α by the RNA-dependent protein kinase PKR. *Cell* 122, 887–900 (2005). [PubMed: 16179258]
19. Hu Z et al. Structural and biochemical basis for induced self-propagation of NLRC4. *Science* 350, 399–404 (2015). [PubMed: 26449475]
20. Zhang L et al. Cryo-EM structure of the activated NAIP2-NLRC4 inflammasome reveals nucleated polymerization. *Science* 350, 404–409 (2015). [PubMed: 26449474]
21. Maekawa S, Ohto U, Shibata T, Miyake K & Shimizu T Crystal structure of NOD2 and its implications in human disease. *Nature communications* 7, 11813 (2016).
22. Yang X et al. Structural basis for specific flagellin recognition by the NLR protein NAIP5. *Cell Res* 28, 35–47 (2018). [PubMed: 29182158]
23. Tenthorey JL et al. The structural basis of flagellin detection by NAIP5: A strategy to limit pathogen immune evasion. *Science* 358, 888–893 (2017). [PubMed: 29146805]
24. Kelley LA, Mezulis S, Yates CM, Wass MN & Sternberg MJ The Pyre2 web portal for protein modeling, prediction and analysis. *Nat Protoc* 10, 845–858 (2015). [PubMed: 25950237]
25. Richards MW et al. An autoinhibitory tyrosine motif in the cell-cycle-regulated Nek7 kinase is released through binding of Nek9. *Mol Cell* 36, 560–570 (2009). [PubMed: 19941817]
26. Qu Y et al. Phosphorylation of NLRC4 is critical for inflammasome activation. *Nature* (2012).
27. Suzuki S et al. Shigella type III secretion protein MxiI is recognized by Naip2 to induce Nlrc4 inflammasome activation independently of Pkcdelta. *PLoS Pathog* 10, e1003926 (2014). [PubMed: 24516390]
28. Krissinel E & Henrick K Inference of macromolecular assemblies from crystalline state. *J Mol Biol* 372, 774–797 (2007). [PubMed: 17681537]
29. Haq T et al. Mechanistic basis of Nek7 activation through Nek9 binding and induced dimerization. *Nature communications* 6, 8771 (2015).
30. Spalinger MR et al. NLRP3 tyrosine phosphorylation is controlled by protein tyrosine phosphatase PTPN22. *J Clin Invest* 126, 1783–1800 (2016). [PubMed: 27043286]
31. Hafner-Bratkovic I et al. NLRP3 lacking the leucine-rich repeat domain can be fully activated via the canonical inflammasome pathway. *Nature communications* 9, 5182 (2018).
32. Moghaddas F et al. Autoinflammatory mutation in NLRC4 reveals a leucine-rich repeat (LRR)-LRR oligomerization interface. *J Allergy Clin Immunol* 142, 1956–1967 e1956 (2018). [PubMed: 29778503]
33. Touitou I et al. Infevers: an evolving mutation database for auto-inflammatory syndromes. *Hum Mutat* 24, 194–198 (2004). [PubMed: 15300846]
34. Duncan JA et al. Cryopyrin/NALP3 binds ATP/dATP, is an ATPase, and requires ATP binding to mediate inflammatory signaling. *Proc Natl Acad Sci U S A* 104, 8041–8046 (2007). [PubMed: 17483456]
35. Jiang X & Wang X Cytochrome c promotes caspase-9 activation by inducing nucleotide binding to Apaf-1. *J Biol Chem* 275, 31199–31203 (2000). [PubMed: 10940292]
36. Song N & Li T Regulation of NLRP3 Inflammasome by Phosphorylation. *Frontiers in immunology* 9, 2305 (2018). [PubMed: 30349539]
37. Barry R et al. SUMO-mediated regulation of NLRP3 modulates inflammasome activity. *Nature communications* 9, 3001 (2018).
38. Py BF, Kim MS, Vakifahmetoglu-Norberg H & Yuan J Deubiquitination of NLRP3 by BRCC3 critically regulates inflammasome activity. *Mol Cell* 49, 331–338 (2013). [PubMed: 23246432]
39. Mangan MSJ et al. Targeting the NLRP3 inflammasome in inflammatory diseases. *Nat Rev Drug Discov* 17, 688 (2018).
40. Khan M, Subramaniam R & Desveaux D Of guards, decoys, baits and traps: pathogen perception in plants by type III effector sensors. *Curr Opin Microbiol* 29, 49–55 (2016). [PubMed: 26599514]
41. Mastronarde DN Automated electron microscope tomography using robust prediction of specimen movements. *J Struct Biol* 152, 36–51 (2005). [PubMed: 16182563]
42. Zheng SQ et al. MotionCor2: anisotropic correction of beam-induced motion for improved cryo-electron microscopy. *Nat Methods* (2017).

43. Rohou A & Grigorieff N CTFIND4: Fast and accurate defocus estimation from electron micrographs. *J Struct Biol* 192, 216–221 (2015). [PubMed: 26278980]
44. Zivanov J et al. New tools for automated high-resolution cryo-EM structure determination in RELION-3. *eLife* 7 (2018).
45. Grant T, Rohou A & Grigorieff N cisTEM, user-friendly software for single-particle image processing. *eLife* 7 (2018).
46. Zhang K Gctf: Real-time CTF determination and correction. *J Struct Biol* 193, 1–12 (2016). [PubMed: 26592709]
47. Wu J et al. Massively parallel unsupervised single-particle cryo-EM data clustering via statistical manifold learning. *PLoS One* 12, e0182130 (2017). [PubMed: 28786986]
48. Kucukelbir A, Sigworth FJ & Tagare HD Quantifying the local resolution of cryo-EM density maps. *Nat Methods* 11, 63–65 (2014). [PubMed: 24213166]
49. Emsley P, Lohkamp B, Scott WG & Cowtan K Features and development of Coot. *Acta Crystallogr D Biol Crystallogr* 66, 486–501 (2010). [PubMed: 20383002]
50. Pettersen EF et al. UCSF Chimera--a visualization system for exploratory research and analysis. *J Comput Chem* 25, 1605–1612 (2004). [PubMed: 15264254]
51. Adams PD et al. PHENIX: a comprehensive Python-based system for macromolecular structure solution. *Acta Crystallogr D Biol Crystallogr* 66, 213–221 (2010). [PubMed: 20124702]
52. Delano WL The PyMol Molecular Graphics System. (2002).
53. Scheres SH RELION: implementation of a Bayesian approach to cryo-EM structure determination. *J Struct Biol* 180, 519–530 (2012). [PubMed: 23000701]
54. Robert X & Gouet P Deciphering key features in protein structures with the new ENDscript server. *Nucleic Acids Res* 42, W320–324 (2014). [PubMed: 24753421]

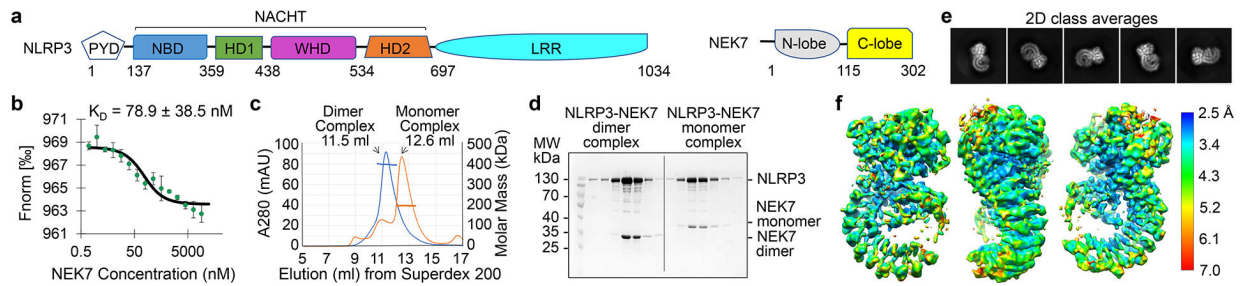


Fig. 1 | Biochemical characterization and cryo-EM structure determination.

a, Schematic domain representation of human NLRP3 and NEK7, with labelled domain boundary defined from this work. **b**, MST analysis of NEK7 binding to NLRP3. A dissociation constant of 78.9 ± 38.5 nM was calculated from three independent replicates (shown as mean \pm s.d.). **c**, Reconstitution of NLRP3-NEK7 dimer and monomer complexes on Superdex 200 gel filtration column (repeated 5 times). Molecular mass distribution within each peak was calculated from in-line MALS measurements, and shown in blue and orange for the dimer and monomer complexes, respectively (Performed once). **d**, SDS-PAGE gels of eluted fractions of dimer and monomer complexes (repeated 5 times). **e**, Representative 2D class averages from the 300 keV cryo-EM dataset, selected amongst 100 classes. **f**, The final cryo-EM density map (shown at 6σ) in three orientations and coloured with local resolutions by ResMap⁴⁸.

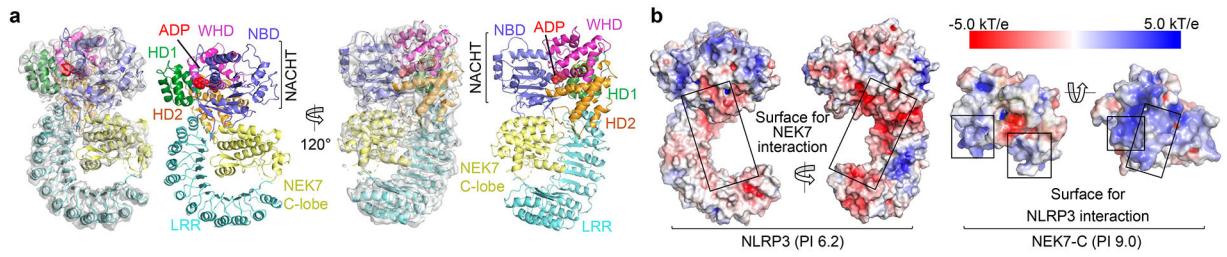


Fig. 2 |. Cryo-EM structure overview.

a Ribbon diagrams of the complex, shown with and without the cryo-EM map (grey, 5σ) in two orientations. Domains are colour coded as in Fig. 1a and the bound ADP is in sphere rendering. **b**, Electrostatic surface representation of NLRP3 and NEK7, colour coded according to electrostatic potential from red (-5.0 kT/e, negatively charged) to blue ($+5.0$ kT/e, positively charged).

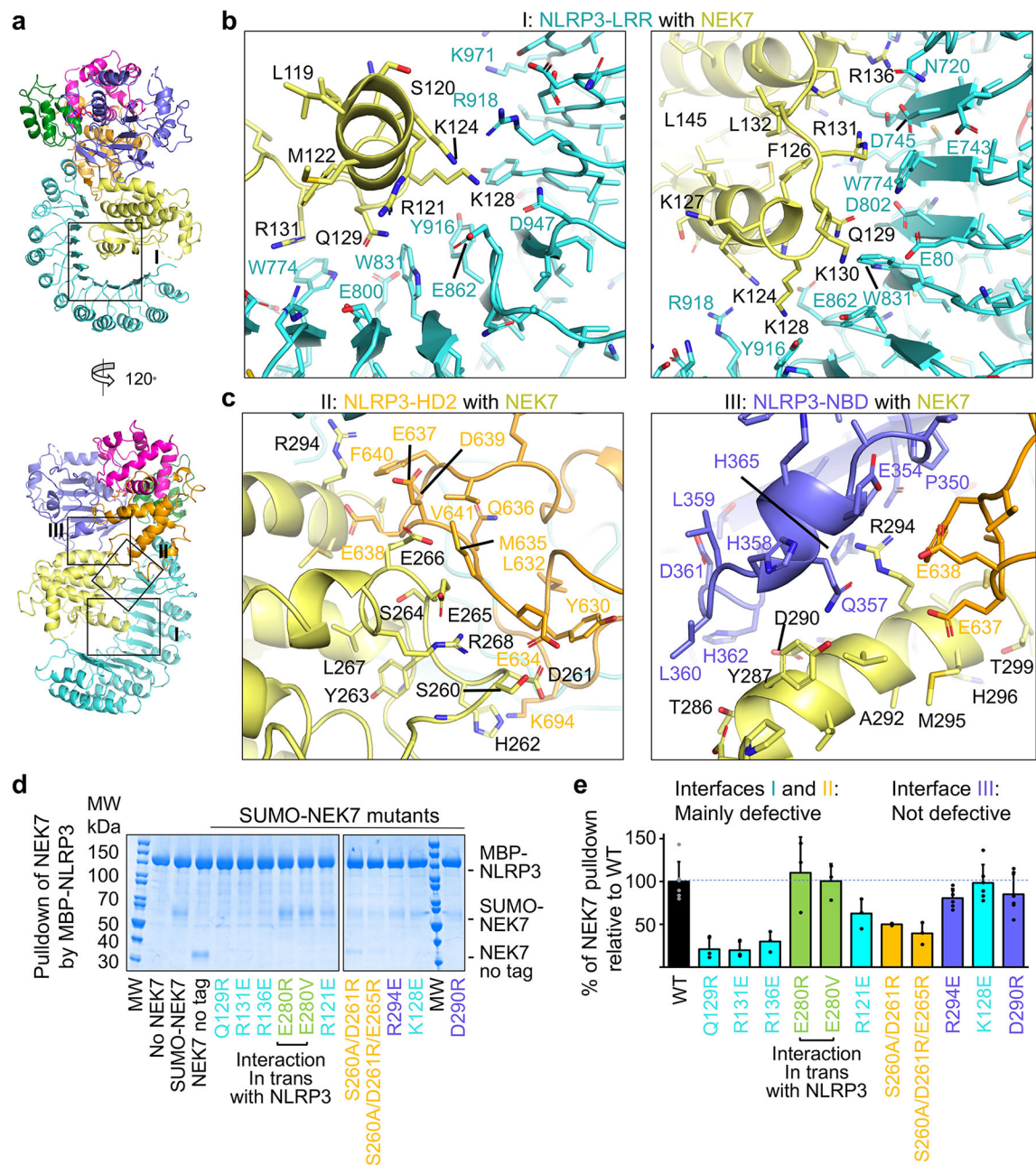


Fig. 3 | Structural insights into NEK7 interaction with NLRP3.

a, The NLRP3-NEK7 complex in two orientations to denote the three interaction regions (I, II and III). **b-c**, Zoom-in views of interaction interfaces between NEK7 and LRR of NLRP3 (**b**) and between NEK7 and HD2 and NBD of NLRP3 (**c**), with main chains in cartoons and side chains in sticks. **d**, Pull-down of purified WT and mutant His-SUMO-tagged NEK7 by purified MBP-tagged WT NLRP3 using amylose resin. Experiments were performed three to six times. NEK7 mutants are coloured by the domain of NLRP3 that they contact with as in (**a-c**). MW: molecular weight markers. **e**, Quantification of mutant NEK7 binding to NLRP3 relative to WT NEK7 (shown as mean \pm s.d. with $n = 3-6$). Dots: individual data points. For gel source data, see Supplementary Figure 1.

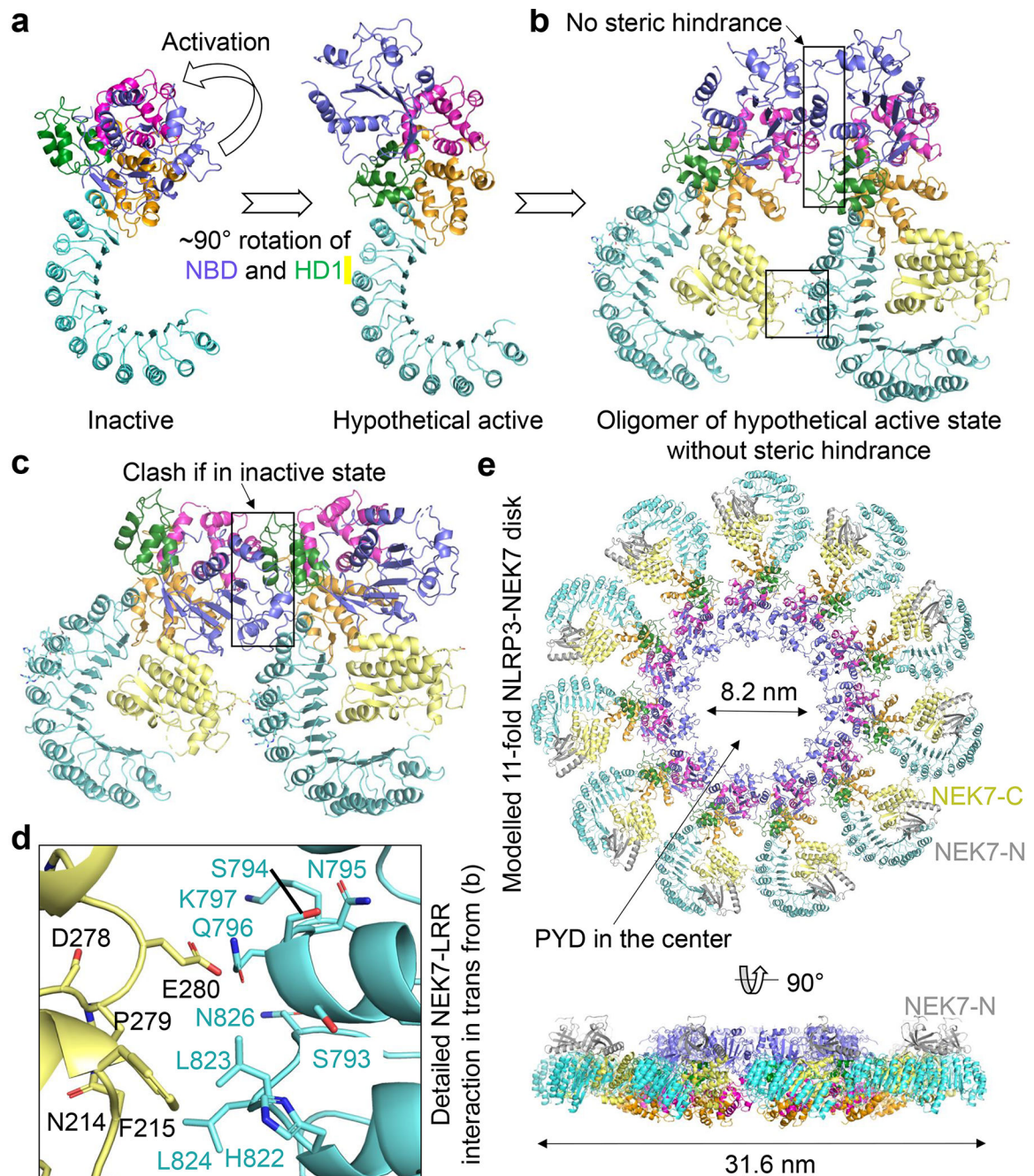


Fig. 5 |. Modelling of active NLRP3 conformation and oligomerization.

a Modelled active NLRP3 (right) from its inactive structure (left) using the activation mechanism of NLRC4 in which NBD-HD1 module rotates by 90° relative to WHD-HD2-LRR module^{19,20}. **b**, A dimer model of the active NLRP3-NEK7 complex based on the NLRC4 disk²⁰. Interaction surfaces are boxed. **c**, A hypothetical inactive NLRP3 dimer would have created steric clashes at multiple sites in the NACHT domain. **d**, Zoom-in view showing the detailed NEK7-LRR interaction in trans boxed in (b). Mutations at this interface compromised NLRP3 inflammasome activation as in Fig. 4. **e**, NLRP3-NEK7

inflammasome disk modelled after the NLRC4 11-subunit disk structure²⁰, shown in two orientations.

Author Manuscript

Author Manuscript

Author Manuscript

Author Manuscript

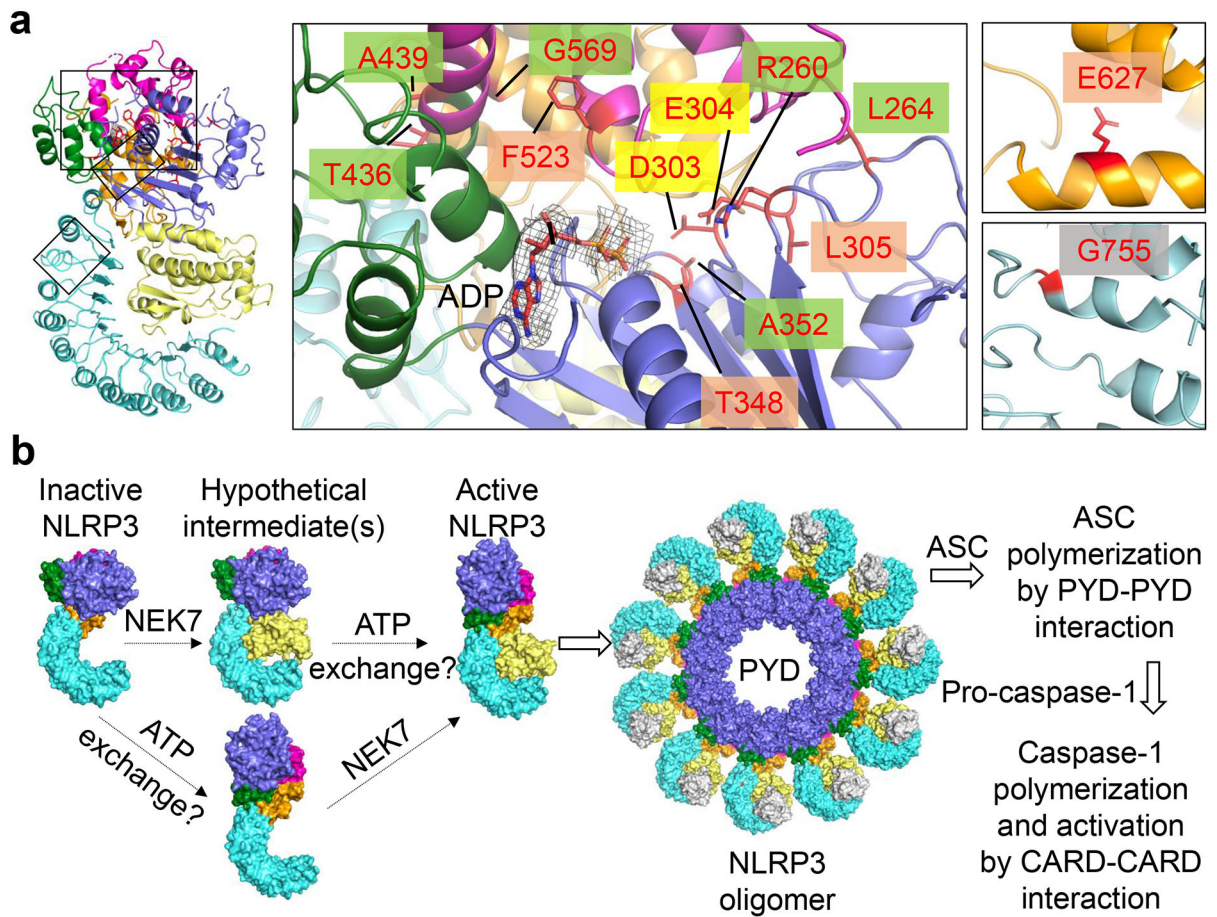


Fig. 6 |. NLRP3 CAPS mutations and model of NEK7-mediated NLRP3 inflammasome activation.

a Structure mapping of all validated pathogenic mutations of NLRP3 from the Infevers website³³, highlighted by background colours behind residue labels. Density for ADP is shown (3σ). Green: disruption of inter-domain interactions in the inactive conformation; mauve: change of local conformation by mutating residues buried within the domains; yellow: alteration in key residues in the Walker B motif; grey: enhancement of NEK7 binding. **b**, A proposed two-step NLRP3 inflammasome activation model.